

# Photodynamics in superfluid helium: Femtosecond laser-induced ionization, charge recombination, and preparation of molecular Rydberg states

A. V. Benderskii, R. Zadoyan, N. Schwentner,<sup>a)</sup> and V. A. Apkarian<sup>b)</sup>

*Department of Chemistry, University of California, Irvine, California 92697*

(Received 6 August 1998; accepted 9 October 1998)

Femtosecond pulses (790 nm) are used for nonresonant laser excitation of superfluid liquid helium to prepare ionic and neutral excited states at energies above 18 eV. Measurements of laser-induced fluorescence and photocurrent enable a detailed description of the primary photoprocesses. A controllable excitation regime unique to femtosecond pulses is realized at laser intensities below the dielectric breakdown threshold,  $I < 5 \times 10^{13}$  W/cm<sup>2</sup>. A steady state of the long-lived triplet excimers He<sub>2</sub><sup>\*</sup>(<sup>3</sup>a) (lowest Rydberg state) is established; the concentration decays between laser pulses through diffusion-controlled bimolecular annihilation to  $\sim 10^{12}$  cm<sup>-3</sup> at a laser repetition rate of 500 Hz. The triplet population is amplified with each pulse in a sequence that involves: (1) ionization of the Rydberg electron of He<sub>2</sub><sup>\*</sup> via complete Coulomb barrier suppression; (2) cascade electron impact ionization of the ground-state He atoms by the ponderomotively accelerated quasifree electrons in liquid He; (3) localization and thermalization of the ‘hot’ electrons and He<sup>+</sup> cations to form electron ‘bubble’ and He<sub>3</sub><sup>+</sup> ‘snowball’ states; (4) recombination of these elementary charge carriers to form He<sub>2</sub><sup>\*</sup>. The amplification factor for the triplets  $M = 2^m$  characterizes the excitation sequence:  $m$  is the number of generations in the cascade ( $m = 5$  at  $I = 4.5 \times 10^{13}$  W/cm<sup>2</sup>), and  $m$  is proportional to the laser intensity and temporal pulse width. The laser-induced ionization cascade prepares an inhomogeneous initial distribution of spatially separated ions on three length scales: clumps of positive charges with an interionic separation determined by the cascade length of 60 Å; a cloud of electrons surrounding the clump at the electron thermalization length  $\sim 10^3$  Å; and interclump separation dictated by the concentration of the He<sub>2</sub><sup>\*</sup> precursors,  $\sim 10^4$  Å. © 1999 American Institute of Physics. [S0021-9606(99)01202-7]

## I. INTRODUCTION

Atomic and molecular spectroscopy in superfluid helium, and in particular, the spectroscopy of impurities isolated in the liquid phase,<sup>1-3</sup> and in large superfluid helium droplets,<sup>4-11</sup> has become the subject of active research in the past few years. A rather thorough review of the experimental and theoretical progress in the field was recently presented by Whaley.<sup>12</sup> A variety of motivations has propelled the recent activity. Due to its unique properties such as chemical inertness, low temperature, and high thermal conductivity, superfluid helium represents an ideal matrix environment<sup>6</sup> for stabilizing weakly bound species and for observing unusual reactions.<sup>6,8,9</sup> Perhaps more tantalizing is the prospect that such studies may lead to a microscopic understanding of superfluidity. The unusual properties of the superfluid phase, hallmarks of which include its vanishing viscosity discovered by Kapitza,<sup>13</sup> extreme thermal conductivity, thermomechanical effect, and second sound,<sup>14</sup> are successfully explained by the phenomenological two-fluid model which was advanced by Tisza<sup>15</sup> and Landau.<sup>16</sup> The classic experiment of Andronikashvili,<sup>17</sup> in which a stack of disks held by a torsion balance was used to observe the decoupling of the superfluid

fraction from the motion, remains the basis of most demonstrations of superfluidity. The microscopic version of this experiment was most convincingly accomplished recently by Toennies and co-workers, in OCS-doped He clusters.<sup>4</sup> With the substitution of the molecular rotor for the disk stack, they were able to spectroscopically observe that the molecule would rotate in the superfluid droplet of <sup>4</sup>He while it would not in <sup>3</sup>He clusters. Moreover, by adding <sup>4</sup>He atoms to the <sup>3</sup>He cluster, the rotation is observed when a layer of about 60 <sup>4</sup>He atoms surrounds the impurity, establishing a microscopic scale for the onset of superfluidity.

Notwithstanding the elegance of these experiments, finite-size effects due to density gradients associated with the surface<sup>18</sup> are a source of concern in these clusters of very broad size distribution.<sup>19</sup> Moreover, it is virtually impossible to control the thermodynamic variables of the cluster (both pressure and temperature), hence, the scrutiny of observables is limited to a single point on the <sup>4</sup>He phase diagram, to  $T = 0.38$  K (Ref. 20) determined by evaporative cooling of the cluster.<sup>21</sup> Analogous measurements of the fluid response to molecular motions, such as vibration, rotation, or electronic excitation, in bulk helium and as a function of temperature, pressure, and phase, are expected to provide broader insights regarding the manifestations of superfluidity on the microscopic scale.

Difficulty in implanting the foreign species in liquid he-

<sup>a)</sup>Permanent address: Institut für Experimentalphysik, Freie Universität Berlin, Arnimallee 14, D-14195 Berlin, Germany.

<sup>b)</sup>Electronic mail: aapkaria@uci.edu

lium has limited studies in the bulk to spectroscopy of metal atoms dispersed in the liquid by laser ablation.<sup>1–3,22</sup> Frequency domain spectra have invariably involved electronic excitations that are strongly coupled to the medium, yielding broadbands with very little information content. Under these conditions, time domain studies can be expected to be significantly more incisive, as has been demonstrated by our group in other studies of impurities isolated in condensed media.<sup>23</sup> Time-resolved studies of molecular probes in bulk superfluid He is our main aim. To this end, instead of injecting foreign molecular species, we rely on intense femtosecond pulses to prepare the microscopic probes in the neat fluid. Femtosecond laser-induced ionization of liquid helium and the subsequent preparation of  $\text{He}_2^*$  excimers in superfluid He are the subjects of this paper. We follow this with a report of time-resolved measurements of the response of the quantum solvent to electronic excitations using the  $\text{He}_2(^3a)$  chromophore.

Motivated by both fundamental considerations and practical applications such as the generation of very high harmonics<sup>24,25</sup> and the production of attosecond pulses,<sup>25</sup> the strong field-induced ionization of atomic He with intense ultrashort laser pulses has been extensively studied. The transition of the process from the multiphoton regime to tunneling ionization,<sup>26–28</sup> and eventually to the complete Coulomb barrier suppression limit,<sup>29</sup> as a function of radiation intensity is well characterized by both experiment and theory. In the case of condensed media, and in particular, in the case of rare-gas clusters where the same physics has been pursued as a potential means for the generation of coherent x rays<sup>30</sup> and highly ionized states of matter,<sup>31</sup> the process is less well understood. Due mainly to its high ionization limit, liquid He enables detailed insights into the photophysics of strong field ionization in condensed media. We demonstrate that the ionization of the liquid proceeds via cascade impact ionization of the ground-state He atoms by electrons accelerated in the intense laser field. Unique to the use of ultrashort pulses is an excitation regime at which a controllable ionization cascade of the liquid can be maintained, below laser breakdown threshold. The controllability of the cascade allows it to be quantitatively characterized both spatially and temporally up to the onset of catastrophic breakdown. A novel mechanism of subcritical (underdeveloped) electron avalanche is advanced based on these observations.

The controlled ionization provides a convenient access to a rich variety of electronic excitations in liquid helium and may prove useful for probing microscopic dynamics in the time domain. The solvation of the nascent ions on picosecond time scales—thermalization of “hot” quasifree electrons to form the bubble state and charge localization and trapping of the parent  $\text{He}^+$  cation to form the snowball state—present valuable models of many-body nonadiabatic dynamics.<sup>32,33</sup> A significant body of work has been dedicated to studies of the thermal ions in superfluid He. The pioneering studies of the mobilities of the excess electron and positive ion<sup>34</sup> showed a surprisingly slow motion of the ions in external electric field, indicating a large effective size. These were followed by theoretical calculations which characterized the microscopic structure of these elementary charge

carriers. In its ground state, the electron is trapped in a large bubble of radius  $\sim 17 \text{ \AA}$ ,<sup>35,36</sup> which is formed due to the strictly repulsive interaction between the electron and He, and the weak interaction between He atoms. This electron-bubble state has been characterized spectroscopically.<sup>37,38</sup> Most recently, there have been theoretical treatments of the dynamics of bubble formation,<sup>39</sup> predicting time scales for the full relaxation from 3.9 to 8.5 ps. Mobility measurements indicate that the positive charge carrier in He is also heavy [with an effective mass of some 30 He atoms (Ref. 40)], depicting the picture of a “snowball” formed by the aggregation of He atoms around the charge center. The core of the snowball when fully vibrationally relaxed may be identified as  $\text{He}_3^+$  from the experiments in He molecular beams<sup>41</sup> and according to recent theoretical simulations of hole migration and self-trapping in small He clusters.<sup>33</sup>

Recombination of the thermal ions leads to the final product of the excitation sequence, molecular Rydberg excimer states  $\text{He}_2^*$ , which lie in the windowless UV range above 18 eV, the lowest excited electronic state being the triplet excimer,  $\text{He}_2(^3a)$ . The existence of these neutral molecular excitations in liquid He was discovered by Surko and Reif.<sup>42</sup> These states have been prepared in the liquid phase through  $\alpha$ -particle and electron-beam bombardment, and their spectroscopy and kinetics have been characterized through both emission and absorption spectroscopy in the IR, visible, and vacuum ultraviolet (VUV) regions,<sup>43–47</sup> which was recently supplemented by studies in clusters using synchrotron radiation.<sup>48</sup> A good summary of the early work can be found in the monograph by Schwentner, Jortner, and Koch.<sup>49</sup> It was established that, similar to the electron-bubble state, the  $\text{He}_2$  excimers exist in stable cavities in liquid helium, with the bubble configuration coordinate responsible for the observed moderate spectral shifts and broadening of transitions within the triplet manifold.<sup>47</sup> Such transitions, therefore, constitute useful probes for time-dependent studies of the response of the quantum solvent.

The organization of this paper is as follows. Section II is devoted to the experimental approach, and in Sec. III the experimental observations are described and analyzed. In Sec. IV we provide a detailed model for the cascade ionization mechanism and show that it quantitatively reproduces all of the relevant experimental measurements. Concluding remarks are given in Sec. V.

## II. EXPERIMENTAL SETUP

The experiments are conducted in a helium cryostat (Oxford) equipped with a set of optical windows. The cold shaft of the cryostat is filled with liquid helium and pumped down to reach a base temperature of  $1.45 \pm 0.05 \text{ K}$ . A wire heater with feedback control allows operation at higher temperature. Most measurements were conducted at base temperature where the best thermal stability is achieved (fluctuations less than 0.01 K). Temperature is measured with a rhodium iron resistor, which was calibrated against the vapor pressure above the liquid.

Femtosecond laser pulses were generated by a laser system consisting of a Ti:sapphire oscillator pumped by an argon-ion laser, followed by a stretcher, regenerative ampli-

fier pumped by a YAG laser, and compressor. The maximum output energy at 790 nm is 500  $\mu\text{J}$  in 80 fs pulses, at a variable repetition rate between 1 kHz and 1 Hz. A few measurements were performed using the second harmonic of the laser at 395 nm. The laser beam is focused in the liquid helium using a single lens, focal length (f.l.)=9 in. The spatial profile of the excitation volume was characterized to extract absolute photoefficiencies. The beam waist was measured in air, in front of the cryostat, using a 10  $\mu\text{m}$  pinhole on an  $X$ - $Y$ - $Z$  translation stage, and determined as the full width at half maximum (FWHM) of  $d=45\pm 5\ \mu\text{m}$  and a length of  $l_{1/2}=1\ \text{cm}$ . Thus, the excitation volume can be estimated as  $1.5\times 10^{-5}\ \text{cm}^3$ .

For time-resolved pump-probe experiments, the femtosecond laser beam was split into two by a 30%–70% single-stack beamsplitter, passed through a variable delay line, and recombined collinearly using another (50%–50%) beamsplitter before the focusing lens. A 1 m translation stage with a corner cube reflector was used to generate optical delays of  $\pm 2\ \text{ns}$ .

To measure lifetimes of long-lived excited states generated by the fs laser, a nanosecond dye laser pumped by a XeCl 308 nm excimer laser (Lambda Physik EMG 101 MSC/FL 2002) was used. An electronic delay generator is used to control the timing between fs pump and ns probe pulses, and the two beams are combined collinearly using a dichroic mirror and focused using the same lens. The time resolution in these measurements is limited to 10 ns by the pulse width of the dye laser.

Fluorescence was collected from the focal spot at a right angle using two collection lenses ( $d=2\ \text{in.}$ , f.l.=5 in.), dispersed through a 1/4 m monochromator, and detected using a photomultiplier tube (PMT). The photon collection efficiency for the arrangement is estimated as  $10^{-5}$ , with the PMT amplification of  $10^7$ , this translates into  $\sim 10^2$  electrons at the anode for every emitted visible photon.

To detect VUV fluorescence from the excitation volume, a gold photocathode with a copper mesh-collecting electrode was fabricated. Given the work function of gold of 4.5 eV, this detector responds to all photons shorter than 275 nm. The photocathode was a  $2\times 2\ \text{cm}$  square gold foil, spaced by 0.4 cm behind the collector. The assembly was situated above the surface of the liquid, 5 cm from the focal spot of the laser. The collection efficiency of this assembly, as determined by the solid angle spanned by the photocathode, is  $\sim 1.3\times 10^{-2}$ . Normally, a positive voltage of +300 V is applied to the collector, and current is measured at the gold electrode using a picoammeter (Keithley model 485). Based on a photoelectron ejection probability of 0.06 for gold,<sup>50</sup> and an estimated electron sweep efficiency of 0.2 (variation of the sweeping voltage from 50 to 500 V resulted in a monotonic increase of the registered current, indicating that saturation is not reached, i.e., not all photoejected electrons are collected), the overall efficiency of  $\sim 2\times 10^{-4}$  collected electrons per emitted VUV photon is estimated.

For detection of ions generated by the femtosecond excitation in liquid helium, we used an assembly of two parallel stainless-steel electrodes immersed in the liquid. Each electrode is a  $2.5\ \text{cm}\times 2.5\ \text{cm}$  square and the separation be-

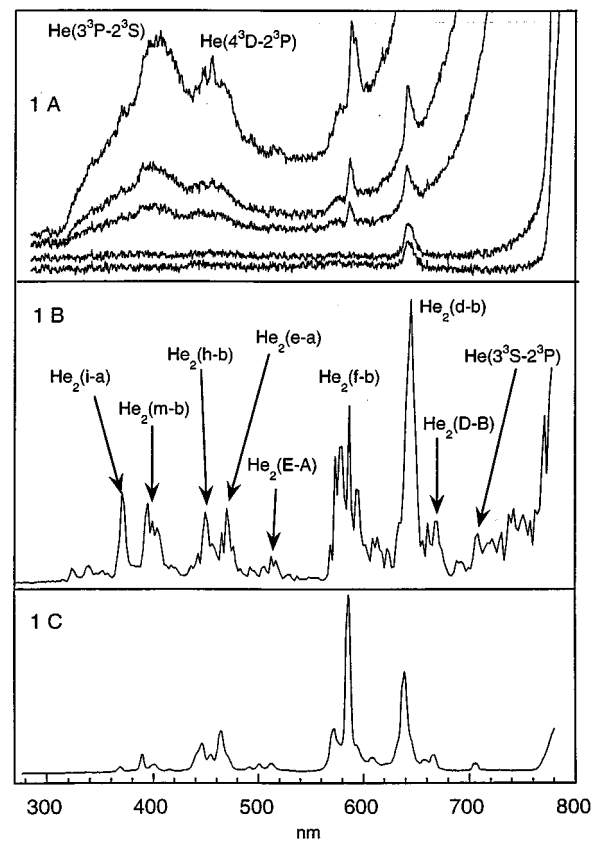


FIG. 1. Emission spectra from liquid helium excited by femtosecond laser pulses. (a) Top three traces: laser intensity above breakdown threshold:  $I = 7.5\times 10^{13}\ \text{W/cm}^2$ ;  $5.9\times 10^{13}\ \text{W/cm}^2$ ;  $5.2\times 10^{13}\ \text{W/cm}^2$ , bottom two traces: below breakdown:  $I = 4.8\times 10^{13}\ \text{W/cm}^2$ ;  $4.4\times 10^{13}\ \text{W/cm}^2$ . (b) Emission spectrum from the liquid helium boiling around the breakdown spot. Broad features of spectra in (a) have been subtracted.  $I = 8\times 10^{13}\ \text{W/cm}^2$ , laser repetition rate is 500 Hz. (c) Emissions from fs laser breakdown in cold He gas (above the surface of the liquid).

tween the electrodes is 1 cm. The laser is focused midgap, therefore,  $\sim 0.5\ \text{cm}$  from either electrode. A sweeping voltage in the range 100–500 V is applied to the lower electrode, and the current measurement is made between the upper electrode and ground using either a picoammeter (Keithley model 485) in cw regime, or a current amplifier (Ithaco model 1211) for resolving the current wave in time.

### III. RESULTS AND ANALYSIS

#### A. Two distinct excitation regimes

Femtosecond laser pulses focused in liquid helium prove to be efficient in producing electronic excitations which manifest themselves in a variety of ways. Specific to the use of ultrashort pulses are two distinct excitation regimes with the demarcation defined by the threshold for dielectric breakdown. While breakdown can be induced with long pulse lasers as well, the regime below breakdown is unique to femtosecond excitation. We are mainly interested in the photophysics in this “low-intensity” regime as a means for controllable preparation of ionic and neutral excited states in liquid helium. Nevertheless, it is useful to contrast observa-

TABLE I. Fluorescence spectrum of liquid helium excited by femtosecond laser pulses in the high- and low-intensity regimes: observed bands and their assignments.

Observed transitions ( $\lambda$ , nm)		Assignment	
Low intensity	High intensity	Atomic	Molecular
	728 m <sup>a</sup>	$3s\ ^1S \rightarrow 2p\ ^1P$	
	707 m <sup>a</sup>	$3s\ ^3S \rightarrow 2p\ ^3P$	
	670 m	$3d\ ^1D \rightarrow 2p\ ^1P$	
640 s <sup>a</sup>	660 m <sup>a</sup>		$D(3s\sigma^1\Sigma_u^+) \rightarrow B(2p\pi^1\Pi_g), (0 \rightarrow 0)$
	640 s <sup>a</sup>		$d(3s\sigma^3\Sigma_u^+) \rightarrow b(2p\pi^3\Pi_g), (0 \rightarrow 0)$
	616 w		$F(3d\delta^1\Delta_u) \rightarrow B(2p\pi^1\Pi_g)$
	612 w		
	610 w		
597 w <sup>c</sup>	598 m <sup>c</sup>		$f(3d\sigma^3\Sigma_u^+) \rightarrow b(2p\pi^3\Pi_g), (0 \rightarrow 0)$
586 w <sup>c</sup>	586 m/s <sup>c</sup>		$f(3d\pi^3\Pi_u) \rightarrow b(2p\pi^3\Pi_g), (0 \rightarrow 0)$
575 m <sup>c</sup>	576 m/s <sup>c</sup>		$f(3d\delta^3\Delta_u) \rightarrow b(2p\pi^3\Pi_g), (0 \rightarrow 0)$
	537 w		? $f \rightarrow b(1 \rightarrow 0)$ ?
	518 m		$E(3p\pi^1\Pi_g) \rightarrow A(2s\sigma^1\Sigma_u^+)$
	505 m	$3p\ ^1P \rightarrow 2s\ ^1S$	
	494 w		? $f \rightarrow b(2 \rightarrow 0)$ ?
470 m	470 m/s		$e(3p\pi^3\Pi_g) \rightarrow a(2s\sigma^3\Sigma_u^+)$
	460 s		$h(4s\sigma^3\Sigma_u^+) \rightarrow b(2p\pi^3\Pi_g), (0 \rightarrow 0)$
	450 m		? $h(4s\sigma^3\Sigma_u^+) \rightarrow b(2p\pi^3\Pi_g)$ ?
	440 s, broad <sup>b</sup>	$4d\ ^3D \rightarrow 2p\ ^3P$	
	404 m/s		$m(5d\sigma^3\Sigma_u^+, \pi^3\Pi_u, \delta^3\Delta_u) \rightarrow b(2p\pi^3\Pi_g)$
	400 m/s		
	395 s		
	395 s, broad	$3p\ ^3P \rightarrow 2s\ ^3S$	
	371 s		$i(4p\pi^3\Pi_g) \rightarrow a(2s\sigma^3\Sigma_u^+)$
	357 w		? $P(6p\pi^1\Pi_g) \rightarrow A(2s\sigma^1\Sigma_u^+)$ ?
352 w			
346 w			
339 m			$l(5p\pi^3\Pi_g) \rightarrow a(2s\sigma^3\Sigma_u^+)$
324 m			$p(6p\pi^3\Pi_g) \rightarrow a(2s\sigma^3\Sigma_u^+)$
315 w			$r(7p\pi^3\Pi_g) \rightarrow a(2s\sigma^3\Sigma_u^+)$

<sup>a</sup>Atomic  $3\ ^1S \rightarrow 2\ ^1P$  and  $3\ ^3S \rightarrow 2\ ^3P$ , and molecular  $^1D(v=0) \rightarrow ^1B(v=0)$  and  $^3d(v=0) \rightarrow ^3b(v=0)$  transitions have been previously characterized in liquid helium excited by electron-beam bombardment by Fitzsimmons and co-workers (Refs. 43 and 44).

<sup>b</sup>Atomic  $3\ ^3P \rightarrow 2\ ^3S$ ,  $4\ ^3D \rightarrow 2\ ^3P$  transitions were observed from the gas-phase plasma bubble formed by pulsed electrical discharge in liquid helium (Ref. 51).

<sup>c</sup>Molecular  $^3f \rightarrow ^3b$ ,  $^3g \rightarrow ^3a$  and  $^3h \rightarrow ^3b$  transitions, previously identified in the gas phase (Ref. 69), have not been reported in the liquid.

tions with those associated with breakdown, which we succinctly relate prior to detailing the measurements of interest.

A sharp intensity threshold for dielectric breakdown is observed at  $I \sim 5 \times 10^{13}$  W/cm<sup>2</sup> for 790 nm pulses (60  $\mu$ J per pulse, 80 fs FWHM, 45 mm beam waist). This threshold, to within 10%, is independent of temperature across the  $\lambda$  point for the measured range, from 1.45 to 2.8 K. The breakdown can be visually identified as a bright spark in the focal volume of the pump beam and is accompanied by: (a) efficient generation of white light centered on the excitation laser wavelength [see the spectrum in Fig. 1(a)]; (b) self-scattering of the pump beam; (c) third-harmonic generation at 264 nm, which propagates collinearly with the pump beam; and (d) cavitation and generation of macroscopic bubbles, which occurs after a time delay of  $\sim 100$   $\mu$ s, as established by scattering of a counterpropagating He-Ne laser focused into the excitation volume. At yet higher intensities, boiling of the liquid around the focal spot can be seen, with ensuing agitation that subsides on a time scale of 0.1 s. The third-harmonic generation and self-scattering indicate that forma-

tion of the plasma responsible for the strong nonlinear optical response occurs within the laser pulse width.

The emission signal obtained above breakdown is very noisy, with a shot-to-shot rms noise of 100%, to be compared with a rms laser intensity jitter of 3%. Characteristic of this regime is a rich spectrum, which contains atomic He\* lines, and both singlet and triplet emissions of He<sub>2</sub>\* excimers. An illustrative set of spectra is provided in Fig. 1. Beside the white light, the spectrum is dominated by the broad emissions at 395 and 445 nm, which can be assigned to  $3\ ^3P \rightarrow 2\ ^3S$  and  $4\ ^3D \rightarrow 2\ ^3P$  atomic Rydberg transitions which are Stark broadened in the high-density plasma.<sup>51</sup> Similar emissions are obtained from transient plasma bubbles created by high-voltage pulsed discharge in liquid helium.<sup>51</sup> Sharper spectroscopic signatures, which include other atomic lines and vibrationally relaxed lines of both singlet and triplet He<sub>2</sub>\* excimers, appear when cavitation and gaseous bubbles resulting from breakdown at high repetition rates persist [see Fig. 1(b)]. The same lines (although somewhat narrower due to the lower plasma density) are also

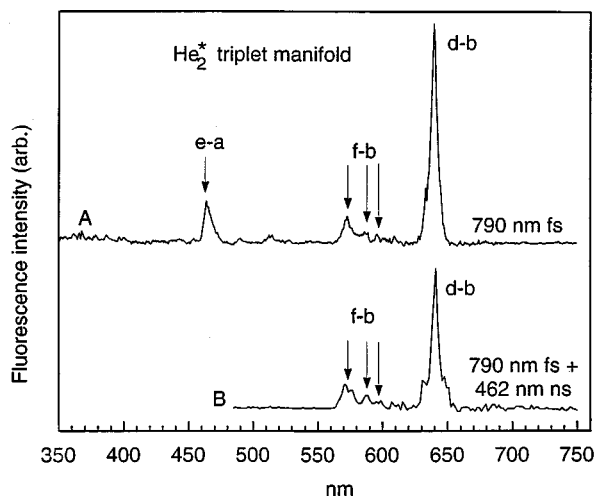


FIG. 2. (a) Fluorescence from liquid helium excited by 790 nm fs laser pulses below breakdown. Laser intensity  $I=4 \times 10^{13}$  W/cm<sup>2</sup>, repetition rate is 500 Hz. (b) Fluorescence induced by 462 nm ns probe laser focused into the excitation volume in liquid helium and delayed 400 ns from the 790 nm fs pump laser (generation), which operates at 500 Hz repetition rate,  $I=4 \times 10^{13}$  W/cm<sup>2</sup>.

observed when breakdown is induced in the cold He vapor just above the liquid level [Fig. 1(c)]. The assignment of lines observed above breakdown are collected in Table I.

The observed visible emission spectra correspond to transitions within the excited Rydberg manifold of atomic and molecular He, among states that lie above 18 eV from ground. It is well established that in the liquid phase, visible fluorescence constitutes a minor fraction,  $10^{-3}$ – $10^{-4}$ , of the overall emission intensity, and that the main relaxation channel is due to radiation from the lowest singlet excited state, the  $\text{He}_2(A \rightarrow X)$  transition, in the 60–100 nm spectral region.<sup>46,52</sup> The number of VUV photons is, therefore, a good estimate of the total number of excimers created in the liquid. Using the gold foil photocathode assembly described in Sec. II, a photocurrent of 40 pA is measured for excitation at a repetition rate of 1 kHz and energy of 100  $\mu\text{J}/\text{pulse}$ , i.e.,  $2.5 \times 10^5$  electrons are collected per pulse. Based on the estimated collection efficiency, this translates into  $\sim 10^9$  VUV photons emitted per laser pulse, indicating an excimer concentration of  $10^{13}$ – $10^{14}$  cm<sup>-3</sup> created in the focal volume. This is  $\sim 100$  times larger than the total number of visible photons emitted, the latter being an estimate based on characteristics of the PMT and collection efficiency of the setup. It is useful to note that one VUV photon is generated per  $4 \times 10^5$  incoming IR photons, i.e., energy conversion efficiency is rather high, of the order of  $10^{-4}$ .

At laser intensities below breakdown, a faint fluorescence appears as a red filament in the liquid. All characteristics of above-breakdown excitation vanish, and the fluorescence spectrum collapses to only three relatively narrow bands as illustrated in Fig. 2. The fluorescence intensity is noticeably more stable, with a shot-to-shot rms noise of 20% (laser noise of 3%). As the temperature of the liquid is raised above the  $\lambda$  point ( $T_\lambda=2.17$  K), the fluorescence intensity drops by  $\sim 1$  order of magnitude. This behavior may be attributed to thermal instabilities caused by the drop in thermal

conductivity upon phase transition, leading to convection currents that disrupt the steady-state population of excimers (*vide infra*). Thus, experimentally, it is found that the controllable excitation below breakdown can only be achieved in the superfluid phase.

Based on the spectral signatures alone (compare spectra in Figs. 1 and 2), it is clear that different channels prevail in the access of the fluorescing states above and below breakdown. Moreover, we establish experimentally that the low-intensity regime is specific to femtosecond excitation. To this end, we used a *Q*-switched pulsed YAG laser of 5 ns pulse width, which was focused in the liquid through a 20 cm lens. The general characteristics of uncontrollable dielectric breakdown induced by the ns laser are similar to that of the fs laser. The emission spectrum obtained from the ns breakdown in the liquid is identical to that in dense He gas [Fig. 1(c)]. Despite the available dynamic range in detection, no emission could be produced below the sharp breakdown threshold. Dielectric breakdown induced in liquid helium using a ns Ruby laser has previously been reported.<sup>53,54</sup> In contrast with the first report,<sup>53</sup> we observe no temperature dependence of the intensity threshold in the range between 1.45 and 4 K. Since the role of impurities in the nanosecond breakdown experiments is well documented,<sup>55</sup> this discrepancy may be attributed to the higher purity of liquid helium in our experiments.

## B. LIF spectroscopy below breakdown

All three of the lines observed in the spectrum below breakdown, Fig. 2, can be assigned to vibrationally relaxed transitions of the  $\text{He}_2^*$  triplet manifold. The strongest band is  $d(3s\sigma^3\Sigma_u^+) \rightarrow b(2p\pi^3\Pi_g)$ , ( $0 \rightarrow 0$ ), at 640 nm; the two weaker bands are a triplet  $f(3d\sigma^3\Sigma_u^+, 3d\pi^3\Pi_u, 3d\delta^3\Delta_u) \rightarrow b(0 \rightarrow 0)$  at 597, 586, and 575 nm, and  $e(3p\pi^3\Pi_g) \rightarrow a(2s\sigma^3\Sigma_u^+)$  ( $0 \rightarrow 0$ ) transition at 470 nm. Only the  $d \rightarrow b$  transition has been observed previously in the liquid.<sup>43</sup> Notable is the absence of the singlet emissions of  $\text{He}_2^*$ , which were readily observed in experiments utilizing particle bombardment<sup>43</sup> and electric discharge.<sup>51</sup> The most intense of the observed lines, the  $d \rightarrow b$  transition, is centered at 639.5 nm, redshifted by 2.1 nm relative to the gas phase, and consists of a line of FWHM=2.5 nm riding over a broad pedestal. These spectral features have previously been interpreted by Dennis *et al.*<sup>43</sup> as unresolved rotational structure manifesting the bubble state nature of  $\text{He}_2^*$  in liquid helium (L-He). We will make extensive use of the  $d \rightarrow b$  fluorescence in our characterization of excitation mechanisms.

The  $d \rightarrow b$  fluorescence decays with a time constant of 25 ns, which corresponds to the radiative lifetime of the  $d$  state in the gas phase.<sup>56</sup> The  $f$  and  $e$  states decay within the detector response time of 10 ns, faster than their gas-phase radiative lifetimes of 20 and 60 ns, respectively.<sup>56</sup> The three emitting states are nested within one  $\text{He}_2^*$  vibrational level ( $e$  is 1110 cm<sup>-1</sup> above  $d$ , and the three substates of the  $f$  state are 1150, 1380, and 1820 cm<sup>-1</sup> above  $d$ ), and are separated from the lower  $c$  triplet excimer state by 1.2 eV. The observed lifetimes imply electronic relaxation on a time scale  $\tau_e \leq 10$  ns from the  $e$  and  $f$  states to the  $d$  state, with the latter

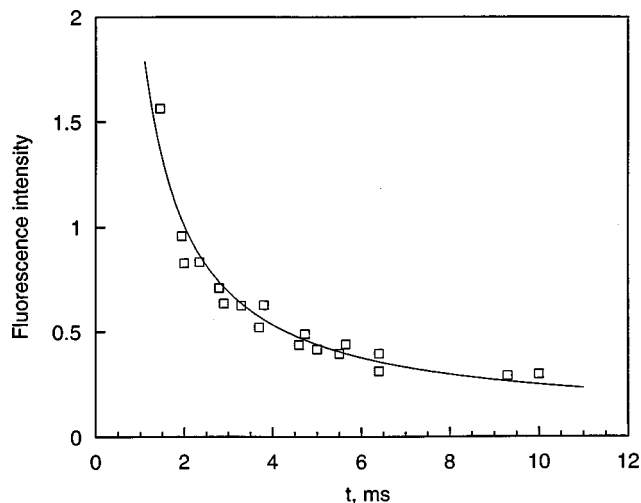


FIG. 3. Intensity of the 640 nm He<sub>2</sub><sup>\*</sup>(*d*→*b*) fluorescence band excited by 790 nm fs pulses vs fs laser repetition rate. Laser intensity below breakdown  $I = 4 \times 10^{13}$  W/cm<sup>2</sup>.  $T = 1.45$  K.

acting as a bottleneck in the electronic cascade. Indeed, fast collisionally induced excitation transfer, with gas kinetic rate constants of the order of  $10^{-10}$  cm<sup>3</sup>/s, is observed among these three states in the gas phase.<sup>56</sup> The important implication of the fast interconversion is that the three observed fluorescence bands may originate from a single excitation transition.

### C. Kinetics

The intensity of the entire fluorescence spectrum below breakdown is inversely proportional to the repetition period of the laser. This is demonstrated in Fig. 3 for the 640 nm emission. Between repetition rates of 1 kHz and 100 Hz, the fluorescence intensity decreases by a factor of  $\sim 10$ . This immediately suggests that the fluorescence results from resonant excitation of a steady state of an intermediate that sur-

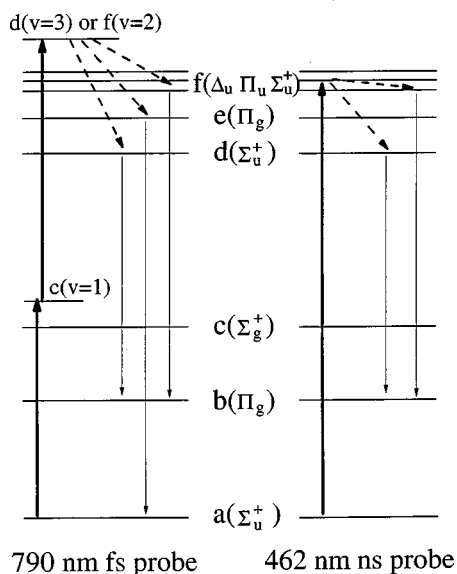


FIG. 4. Energy-level diagram of He<sub>2</sub><sup>\*</sup> triplet manifold.

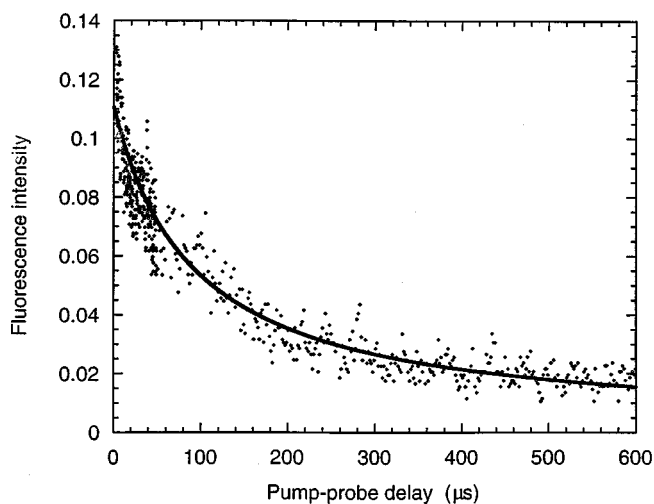
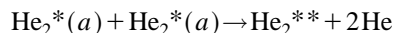


FIG. 5. Intensity of the 640 nm He<sub>2</sub><sup>\*</sup>(*d*→*b*) fluorescence induced by 462 nm ns probe laser vs delay between fs pump (generation) and ns probe pulses. Intensity of the fs pump laser is below breakdown.  $T = 1.45$  K. Solid line: fit to Eq. (1).

vives between laser pulses. The only candidate is the lowest triplet excimer state He<sub>2</sub>(<sup>3</sup>*a*), the lifetime of which in liquid helium is known to be determined by diffusion-controlled bimolecular annihilation



with a bimolecular rate constant of  $K = 5.5 \times 10^{-10}$  cm<sup>3</sup>/s at  $T = 1.45$  K as determined by Fitzsimmons and co-workers.<sup>44</sup> Two-photon excitation of He<sub>2</sub>(<sup>3</sup>*a*) at 790 nm would lead to the observed set of triplet states, as illustrated in Fig. 4. Resonant excitation of the steady-state triplet would explain the absence of the single states in the fluorescence spectrum in Fig. 2.

The suggested mechanism of fluorescence excitation is directly verified by pump-probe experiments, where the fs laser is used to generate excimers, and a 10 ns dye laser is tuned to the <sup>3</sup>*e*←<sup>3</sup>*a* transition at 462 nm to probe the He<sub>2</sub>(<sup>3</sup>*a*) population (see the energy-level diagram in Fig. 4). As expected, due to the fast interconversion from <sup>3</sup>*e* to <sup>3</sup>*f* and <sup>3</sup>*d* states, the fluorescence spectra obtained using this femtosecond pump-nanosecond probe scheme [Fig. 2(b)] are identical to those from 790 nm femtosecond pulses alone (the *e*→*a* emission is masked by the probe laser). The fluorescence intensity was verified to be linear with the probe intensity, demonstrating one-photon excitation. The laser-induced fluorescence (LIF) intensity (640 nm) exhibits the expected bimolecular decay as a function of the delay between the femtosecond pump and nanosecond probe pulses. This is shown in Fig. 5 by the fit of the data at  $T = 1.45$  K to the form:

$$\frac{I(t)}{I_0} = \frac{C(t)}{c_0} = \frac{1}{1 + KC_0 t}, \quad (1)$$

in which  $I_0$  and  $C_0$  designate, respectively, the fluorescence intensity and He<sub>2</sub>(<sup>3</sup>*a*) concentration at  $t = 0$ . This experiment defines  $t = 0$  within the probe pulse width of 10 ns; the absence of a rise in the data establishes that the formation of

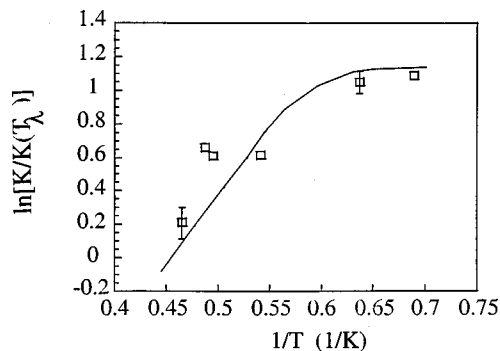


FIG. 6. Temperature dependence of the decay rate determined from the fit of the fs pump–ns probe kinetics in Fig. 5. Solid line: results of Fitzsimmons *et al.* (Ref. 44).

$\text{He}_2(^3a)$  is completed in this time period. Using the bimolecular annihilation constant  $K$  of Fitzsimmons *et al.*,<sup>44</sup> an initial concentration of  $C_0 \approx 10^{13} \text{ cm}^{-3}$  is extracted from the fit.

The temperature dependence of the measured rate constant is shown in Fig. 6. The data are in good agreement with those of Fitzsimmons *et al.*<sup>44</sup> (solid line in Fig. 6). The rate constant exhibits the characteristic inverted Arrhenius temperature dependence with an activation energy of 8.3 K, corresponding to the roton minimum in the dispersion curve. This dependence below the  $\lambda$  point is expected, since diffusion of impurities through the superfluid is hindered only by scattering on the thermal population of rotons. The agreement of our data with the prior measurements further implies that the femtosecond excitation is “gentle” and does not significantly affect the temperature and transport properties of the fluid in the excitation volume.

The same bimolecular kinetics reproduces the repetition rate dependence of the fluorescence induced by the femtosecond laser alone, as demonstrated in Fig. 3. The second-order curve calculated using  $C_0$  extracted from the fs pump–ns probe kinetics is represented by the solid curve in Fig. 3 and shows excellent agreement with the data. Slowing down of the diffusion at higher temperature implies that more triplets will survive and be available for reexcitation. This is indeed observed: as the temperature is increased from  $T=1.5 \text{ K}$  to  $T=2.1 \text{ K}$ , the steady-state fluorescence at 500 Hz increases by a factor of  $\sim 2$ .

The observed kinetics and the absence of the singlet  $\text{He}_2^*$  emission lines imply that the fluorescence is *only* the result of excitation of the excimers which survive from the prior pulse, which after a time delay of  $t_1=1-2 \text{ ms}$  reach a concentration of  $C(t_1)=10^{12} \text{ cm}^{-3}$ . To access the coupled manifold of  $\text{He}_2(d, e, f)$  states, two photons at 790 nm are required, which are illustrated in Fig. 4. A near-resonant real intermediate can be assigned to this two-photon excitation by noting that the  $1 \leftarrow 0$  vibrational band of the  $c(3p\sigma^3\Sigma_g^+) \leftarrow a(2s\sigma^3\Sigma_u^+)$  transition is centered at 805 nm with a FWHM of 10 nm in LHe.<sup>47,44</sup> The second photon would then overlap the  $d(3s\sigma^3\Sigma_u^+, v=3) \leftarrow c(v=1)$  transition, which is centered at 780 nm in the gas phase, and the nearby  $f(v=2) \leftarrow c(v=1)$  transitions which in the gas phase occur at 803 and 817 nm for the  $f(3d\pi^3\Pi_u)$  and  $f(3d\sigma^3\Sigma_u^+)$  com-

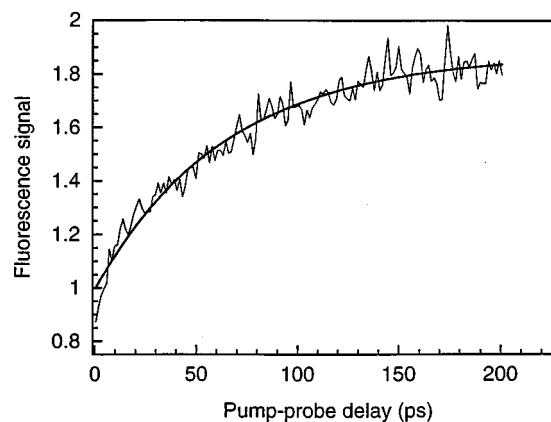


FIG. 7. Generation dynamics of the  $\text{He}_2^*(^3a)$  excimers: pump–probe 790 + 790 nm induced fluorescence [640 nm,  $\text{He}_2^*(d \rightarrow b)$ ] as a function of delay between generation ( $W_{\text{pu}}=50 \mu\text{J/pulse}$ ) and probe ( $W_{\text{pr}}=25 \mu\text{J/pulse}$ ) pulses.

ponents. The broad spectral profiles of the fs laser (FWHM  $\sim 10 \text{ nm}$ ) and absorption lines in liquid He, the large transition dipoles involved, and the high intensities of the excitation pulses, assure an efficient resonant two-photon excitation.

#### D. Excimer formation time

Utilizing the two-photon fluorescence excitation scheme of the  $\text{He}_2(^3a)$  excimers, their formation dynamics were monitored in real time with femtosecond resolution in a single-color 790 nm+790 nm pump–probe experiment. The first pulse (nonresonantly) starts the generation dynamics, and the second, delayed pulse, probes the produced concentration of the lowest state triplets  $\text{He}_2(^3a)$ , as pictured in Fig. 4. The 640 nm ( $d \rightarrow b$ ) fluorescence intensity was recorded as a function of pump–probe delay and is characterized by a fast initial rise on the 100–200 ps time scale, which is shown in Fig. 7. This is followed by a slower growth which continues for several nanoseconds. Quantitative studies of this kinetic stage are complicated by the beam walk-off problems associated with the long optical delay. Finally, with a 2 ns

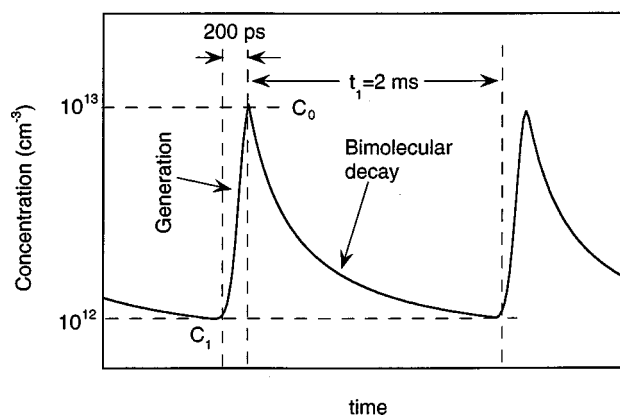


FIG. 8. Evolution of the concentration of  $\text{He}_2^*(^3a)$  excimers in the steady-state regime realized at laser repetition rate 500 Hz below breakdown.

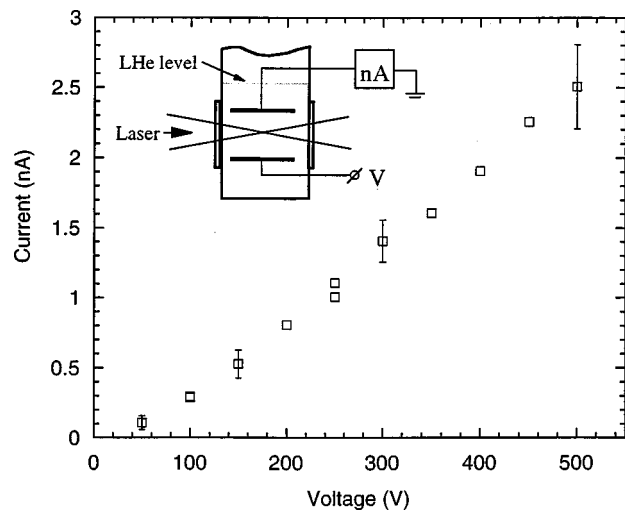


FIG. 9. Photocurrent through liquid helium excited by fs laser induced by applied voltage. Inset: experimental geometry.

time delay between pulses, it is verified that the dependence of the fluorescence intensity on the probe power is quadratic.

### E. Steady state of $\text{He}_2(^3a)$ excimers

The schematic reconstruction of the experimentally determined concentration profile  $C(t)$  is shown in Fig. 8. During the dark time between laser pulses  $t_1 = 2$  ms for the typically used 500 Hz repetition frequency, the excimers decay according to Eq. (1), from the initial concentration  $C_0$  generated within several ns of the laser pulse, to  $C_1 = C_0 / (1 + KC_0 t_1)$ . Because  $C_0$  is of the order of  $10^{13} \text{ cm}^{-3}$  and  $K = 5.5 \times 10^{-10} \text{ cm}^3/\text{s}$  at  $T = 1.45 \text{ K}$ ,  $KC_0 t_1 \gg 1$  for  $t_1 \geq 1$  ms, and concentration  $C_1$  of triplets surviving until the next laser pulse is a robust number:  $C_1 \approx 1/Kt_1 = 10^{12} \text{ cm}^{-3}$  independent of  $C_0$ . Thus, the bimolecular decay acts as a noise reduction mechanism for the steady-state concentration. Since the formation time of the excimer is much longer than the pulse width of the laser, the fluorescence intensity from the single pump beam measures the concentration  $C_1$  of excimers generated by the previous pump pulse, whereas fluorescence induced by a probe pulse delayed by  $\sim 2$  ns from the generation pump pulse detects concentration  $C_0$  created by the pump. To maintain the steady state, the pump pulse must amplify the excimer population from  $C_1$  to  $C_0$ . The rest of the measurements are aimed at characterization of the mechanism involved in this process.

### F. Photocurrent measurements

Given the fact that radiation far from resonance is used to prepare the observed excimer states, it may be suspected that ionization is the first step in the process. While ionization is self-evident above breakdown, by direct measurements of photocurrent we establish that ionization occurs below breakdown as well.

When the femtosecond laser operating at 1 kHz is focused between two parallel electrodes separated by 1 cm, at a sweeping voltage of a few hundred volts applied to the lower electrode (see the inset in Fig. 9), current in the pico-

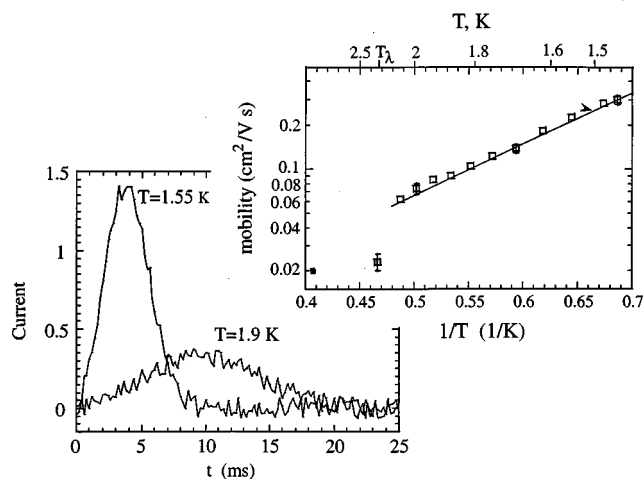


FIG. 10. Time-resolved current wave and temperature dependence of the mobility for the negative charge carrier. Solid line: data of Mayer and Reif for the mobility of electron in L-He (Ref. 34).

to nanoampere range is detected on the upper electrode. Current is detected at laser intensities both above and below breakdown. At a fixed laser power, the current increases monotonically with applied voltage, up to 500 V/cm, as shown in Fig. 9. The absence of saturation in the  $I$ - $V$  curve indicates that only a small fraction of the charges produced by the laser is extracted. Consistent with this, the applied voltage does not modify the fluorescence intensity. Based on the signal-to-noise ratio of fluorescence, we can establish an upper limit for the fraction of extracted ions as 3%. Further, this observation establishes that the excitation mechanism does not involve preexisting ions, since such would be swept away by the applied voltage.

Time-resolved measurements of the current wave yield the mobility of the charge carriers and their identification as the thermal electron bubble and the positively charged snowball. The current wave was recorded with the laser operating at 30 Hz to extend the time scale to  $\sim 30$  ms. In Fig. 10 we show the time-resolved current wave for the negative charge carriers at two different temperatures. The arrival time of the peak of the wave is a linear function of the applied voltage. The width of the wave is equal to the peak arrival time, indicating that the collected charge cloud expands to a diameter comparable with the travel length (5 mm). The average drift velocity can be calculated from the peak arrival time (140 cm/s at 1.55 K and 50 cm/s at 1.9 K for the traces in Fig. 10). The extracted mobility of the charge carriers as a function of temperature between 1.5 and 2.2 K is presented in Fig. 10. Below the  $\lambda$  point, the data are well described by an inverse Arrhenius law with an activation energy of  $8.38 \pm 0.10 \text{ K}$ , in accordance with the general mechanism of diffusion and mobility in superfluid helium. The data are in excellent agreement with the experiments of Mayer and Reif<sup>34</sup> (solid line in Fig. 10) who have previously measured mobilities of the thermalized charge carriers in liquid helium.

### G. Power dependence of the fluorescence and photocurrent

The most important data regarding the photogeneration mechanism is provided by the power dependence of photo-

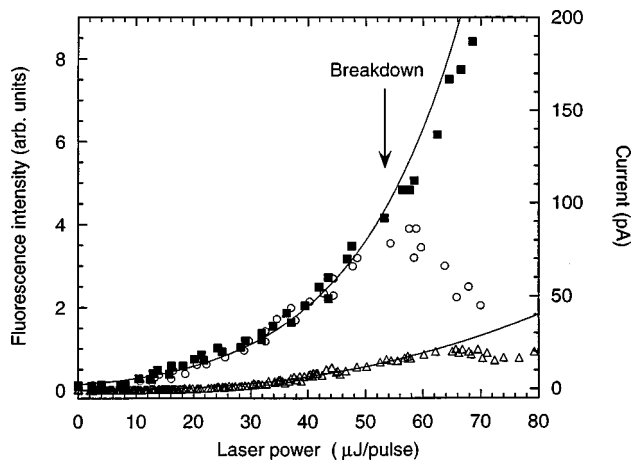


FIG. 11. Power dependence of the 640 nm  $\text{He}_2^*(d \rightarrow b)$  fluorescence and photocurrent: (a) open triangles, fluorescence from pump beam alone; (b) open circles, fluorescence from 790 nm probe pulse ( $W_{\text{pr}} = 26 \mu\text{J/pulse}$ ) as a function of the pump pulse power; and (c) filled squares, photocurrent as a function of pump pulse power.

current and fluorescence, which we carry out simultaneously. The results of this measurement at a laser repetition frequency of 500 Hz are collected in Fig. 11. Fluorescence is measured under two different modes of excitation:

(a) The open triangles in Fig. 11 show fluorescence due to the pump beam alone, which measures the concentration  $C_1$  of the  $\text{He}_2^*(^3a)$  excimers that survive from the previous pulse (see Fig. 8).

(b) The open circles (Fig. 11) represent fluorescence induced by a 790 nm probe pulse of fixed intensity (laser energy per pulse  $W = 26 \mu\text{J/pulse}$ ) delayed by  $\sim 2$  ns from the 790 nm pump pulse of varying intensity. According to the  $\text{He}_2^*(^3a)$  formation kinetics described in Sec. III D, this delay ensures that the probe pulse measures the population  $C_0$  of the excimers created by the 790 nm pump pulse.

Note, in both cases (pump alone and pump+probe), the fluorescence signal decreases above the breakdown threshold (marked by an arrow) due to laser scattering from the plasma.

The current recorded simultaneously with the pump-probe fluorescence intensity is shown by filled squares in Fig. 11. Below breakdown, the power dependence current and fluorescence are identical, which indicates that the production of spatially separated ions is a key step in the triplet generation mechanism. Just below breakdown, at a laser intensity of  $I = 4 \times 10^{13} \text{ W/cm}^2$ ,  $10^6$  charges are extracted with an applied voltage of 200 V. Comparison of this number with the excimer concentration, which was independently estimated from the fluorescence signal intensity and from the bimolecular kinetics as  $C_0 \sim 10^{13} \text{ cm}^{-3}$  in an excitation volume of  $2 \times 10^{-5} \text{ cm}^3$ , gives the probability of ion separation by the external electric field of  $P \sim 5 \times 10^{-3}$ . This in turn has important implications regarding the initial separation of the ion pairs produced by the generation pulse.

The power dependence of the generation step was further characterized by stretching the pulse width of the pump laser. Stretching the pulse from 80 to  $\sim 250$  fs, while keeping the total energy per pulse constant, at  $W = 50 \mu\text{J}$ , does not

change either the fluorescence intensity, or photocurrent. This behavior is a signature of a controlled field-induced avalanche ionization (see the discussion section), and suggests that we dismiss from consideration any multiphoton process in the generation mechanism.

The above data allow the characterization of the photo-physics once the triplet steady state is reached. The number of pulses required to reach the steady state at a given repetition rate is an inherently difficult determination since it requires single-shot measurements. We could establish that at a repetition rate of 500 Hz, and at a laser intensity of  $I = 4.5 \times 10^{13} \text{ W/cm}^2$ , the steady state is reached within five pulses.

#### IV. DISCUSSION

The presented experimental observations clearly demonstrate that femtosecond laser excitation of liquid helium, far from any resonances, enables efficient access of neutral and ionic states that lie at energies above 18 eV. The regime of controllable excitation, which is realized at intensities below laser breakdown, occurs in the superfluid phase when irradiated at sufficiently high repetition rates to establish a steady-state concentration of the triplet excimer,  $\text{He}_2(^3a)$ . The experimentally determined time profile of the  $^3a$  excimer concentration was illustrated in Fig. 8. The concentration decays via diffusion-controlled self-annihilation to  $C_1$ , and is amplified by a factor of  $\sim 10$  by the laser pulse to reach  $C_0$ . The data in Fig. 11 established that the power dependence of the photogeneration of excimers and that of photocurrent are identical. This naturally leads to the conclusion that laser-induced ionization followed by recombination of ion pairs is the mechanism of excimer formation. Below, we develop a model for autocatalytic amplification of the excimer concentration by a laser-driven electron avalanche ionization. Consecutive steps of the mechanism are detailed in the sections that follow: initial ionization of preexisting excimers, controlled electron avalanche, and thermalization and recombination of the generated ions. The model uniquely allows us to quantitatively reproduce all relevant experimental observables in this controlled excitation regime.

##### A. Ionization of excimers via Coulomb barrier suppression

The relatively weak power dependence of photocurrent observed in Fig. 11, rules out photoionization of ground-state He atoms. At the intensities used in our experiments, laser ionization of ground-state helium would be expected to be in the multiphoton regime ( $\sim 16$  photons at 790 nm,  $h\nu = 1.55 \text{ eV}$ ).<sup>57</sup> The transition from the perturbative multiphoton picture to tunneling ionization is determined by the Keldysh adiabaticity parameter<sup>58</sup>

$$\gamma = \left( \frac{\text{I.P.}}{U_p} \right)^{1/2} = \left( \frac{\text{I.P.}}{e^2 F_0^2 / 2m_e \omega^2} \right)^{1/2},$$

where I.P. = 24.6 eV is the ionization limit of He, and  $U_p$  is the ponderomotive potential of an electron in the laser electric field  $F = F_0 \cos(\omega_0 t)$ . For atomic He, the switch over

from the multiphoton ( $\gamma \ll 1$ ) to the tunneling ( $\gamma \gg 1$ ) regime occurs at field intensities of  $\sim 2 \times 10^{14} \text{ W/cm}^2$ , which is an order of magnitude higher than our experimental intensities. Indeed, extrapolation of the He ionization probability by femtosecond laser pulses measured in the gas phase<sup>27</sup> to our range of intensities predicts that ionization probability changes by  $\sim 4$  orders of magnitude for a twofold increase in laser intensity. We would not expect a dramatic change in this behavior from gas to liquid. Therefore, the observed weak dependence of photocurrent on laser intensity cannot be ascribed to photoionization of ground-state He.

Consider instead the  $\text{He}_2(^3a)$  excimers, which are present at concentration  $C_1 \sim 10^{12} \text{ cm}^{-3}$  in the focal volume at the time a laser pulse arrives. The applied laser intensities are now sufficient to completely suppress the Coulombic potential that binds the Rydberg electron. Complete suppression of the Coulomb barrier occurs above the critical electric field<sup>29</sup>

$$F_{\text{th}} = \frac{(\text{I.P.})^2}{4e^2},$$

which in the case of  $\text{He}_2^*(^3a)$ , with  $\text{I.P.} = 4.26 \text{ eV}$ , would correspond to a laser intensity threshold  $I_{\text{th}} \approx 1.5 \times 10^{12} \text{ W/cm}^2$ . Since the experiments are carried out at intensities which are an order of magnitude above this threshold, within the laser pulse, the Rydberg electron is "quasi-free." Equivalently, the ionization probability of  $\text{He}_2(^3a)$  is  $\sim 1$  even at the lowest laser intensity used in the experiments, therefore, in effect independent of laser power.

Ionization of the excimer is not sufficient to account for the steady-state kinetics, nor is it sufficient to account for the intensity dependence of the photocurrent. The radiation must now amplify the number of ions produced by ionization of excimers that survives from the prior pulse. Collision-assisted energization of quasifree electrons in liquid helium driven by the ponderomotive force of the radiation field, and subsequent impact ionization of ground-state He atoms by the energized electrons, can lead to an ionization cascade in which the initial excimer concentration is multiplied, as we describe next.

## B. Controlled electron avalanche ionization

The mechanism of cascade electron impact ionization, responsible for the extensively studied nanosecond breakdown in dense gas and condensed media, was first proposed in a theoretical paper by Zel'dovich and Raizer.<sup>59</sup> The formulation has been shown to provide a quantitative description of nanosecond breakdown in dense helium gas and can be adapted to the present case.<sup>53</sup> Briefly, electrons are accelerated by the electric field and gain kinetic energy in collisions with He atoms. The collisions are necessary for the simultaneous conservation of energy and momentum. Because of the mass asymmetry between electron and atom, the elastic collisional energy loss is small and can be neglected in the description of the process (energization of the electrons may occur at field amplitudes above  $\sim 10^6 \text{ V/cm}$ ,<sup>60</sup> i.e., for laser intensities  $> 10^9 \text{ W/cm}^2$ ). Electron impact ionization occurs when the electrons reach a kinetic energy above

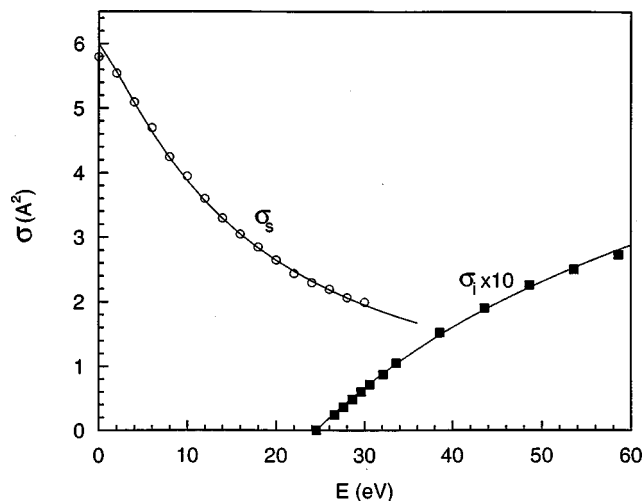


FIG. 12. (A) scattering cross sections of an electron on a He atom; (B) electron impact ionization cross section of He.

the He ionization potential. The secondary (low-energy) electrons are in turn accelerated by the same mechanism, leading to the ionization cascade. Scrutiny of the dynamics of these processes, presented below, will allow comparison with the experimentally measured power dependences of the fluorescence and photocurrent (Fig. 11) and implications about the initial spatial distribution of the generated ions.

The classical expression for the rate of energy gain by an electron in the radiation field

$$K_{\epsilon}(\epsilon) = \frac{d\epsilon}{dt} = \frac{e^2 F_0^2}{2m_e(\omega_0^2 + \nu_{\text{coll}}^2)} \nu_{\text{coll}} = U_p \frac{\omega_0^2}{\omega_0^2 + \nu_{\text{coll}}^2} \nu_{\text{coll}}, \quad (2)$$

describes the average energy transferred from radiation to electron per collision, times the collision frequency  $\nu_{\text{coll}}$  (note that we use the space-averaged value of the field intensity  $F_0$ ). The picture is one of elastic collisions that randomize the direction of the electron momentum, and therefore, its projection on the field direction, leading to a random walk in three-dimensional momentum space, with the step size of the walk determined by the laser intensity. The root-mean-momentum ( $\langle p^2 \rangle$ )<sup>1/2</sup> gain is proportional to the square root of the number of collisions, and therefore, the energy gain is proportional to the number of collisions. The high density of the liquid and the absence of energy-loss channels for electrons below 20 eV provide favorable conditions for fast energization. At a laser intensity  $I = 4 \times 10^{13} \text{ W/cm}^2$ , i.e., space-averaged electric-field  $F_0 = 1.2 \text{ V/\AA}$ , the amplitude of  $e^-$  oscillation is  $x_0 = eF_0 / (2m_e \omega_0^2) = 3.7 \text{ \AA}$ , which is comparable to the interatomic separation in L-He. These conditions are different from the case of dense helium gas, which was originally considered by Zel'dovich and Raizer<sup>59</sup> in their laser breakdown theory. In the liquid, the electron collision frequency may be comparable or even higher than the light frequency  $\omega_0 = 2.4 \times 10^{15} \text{ s}^{-1}$ . As a consequence, the average energy gain per collision may be less than the ponderomotive potential, which is reflected by the factor  $\omega_0^2 / (\omega_0^2 + \nu_{\text{coll}}^2)$  in Eq. (2).

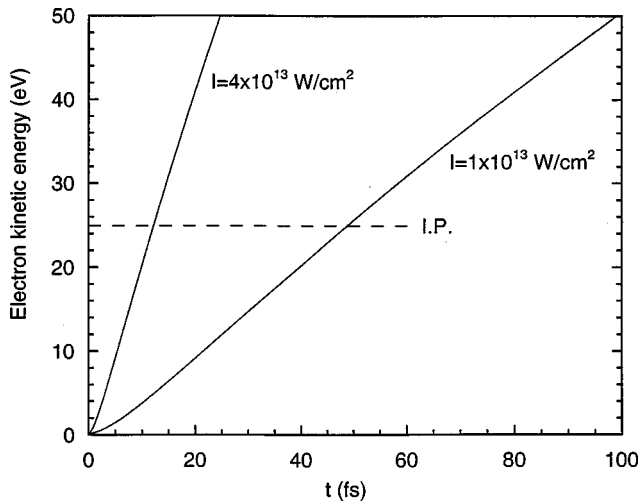


FIG. 13. Energy-gain dynamics of an electron in liquid helium in a laser field: numerical solution of Eq. (2) using scattering cross-section  $\sigma_s(\epsilon)$  from Eq. (4).

The collision frequency is a function of the kinetic energy, since it is determined by the electron velocity  $v_{el}$  and the mean-free path of the electron  $l_s$ :

$$\nu_{coll} = v_{el}/l_s(\epsilon) = n\sigma_s(\epsilon) \sqrt{\frac{2\epsilon}{m_e}}. \quad (3)$$

The momentum scattering cross section of low-energy electrons on He  $\sigma_s(\epsilon)$ , which was measured as a function of energy in the gas phase,<sup>61</sup> is shown in Fig. 12(A). The data can be fitted to the form [solid line in Fig. 12(A)]

$$\sigma_s(\epsilon) = \frac{1}{0.165 + 0.0056\epsilon^{1.2119}} (\text{\AA}^2), \quad (4)$$

where  $\epsilon$  is in eV, which we used in our calculations. The cross section decreases from  $(5.5 \pm 0.1) \text{\AA}^2$  at 0–1 eV to  $2.3 \text{\AA}^2$  at 25 eV.

If we substitute Eq. (3) into Eq. (2) and solve the resulting differential equation, we obtain a kinetic-energy gain curve for a quasifree electron in L-He in a laser field. The results of numerical integration using the fitted experimental dependence (4) for  $\sigma_s(\epsilon)$  are shown in Fig. 13. The curve is superlinear in the beginning, reflecting the increasing collision frequency as the electron is accelerated. In spite of some complicating details (*vide infra*), Eq. (2) and the dynamics pictured in Fig. 13 demonstrate the most important physical features of the model. The energy gain rate, which determines the number of generations in the cascade developed during the laser pulse, is proportional to the ponderomotive potential, which in turn is proportional to the laser intensity:

$$U_p \text{ (eV)} = \frac{I \text{ (W/cm}^2\text{)}}{2 \times 10^{13}}.$$

(for a 790 nm wavelength). Thus, as illustrated in Fig. 13, it takes four times longer to reach energy above the I.P.(He) at  $I = 1 \times 10^{13} \text{ W/cm}^2$  than at  $4 \times 10^{13} \text{ W/cm}^2$ .

Above 25 eV, an electron ionizes the He atom with a finite probability determined by the impact ionization cross-section  $\sigma_i(\epsilon)$ . The latter increases sharply from 0 at I.P. to a

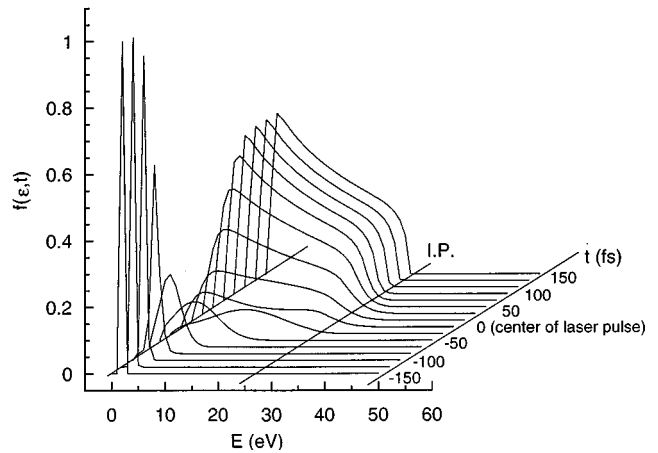


FIG. 14. Time evolution of the electron energy distribution function  $f(\epsilon, t)$  during the laser pulse: numerical solution of Eq. (5). Laser pulse of FWHM=80 fs and peak intensity  $I = 3 \times 10^{13} \text{ W/cm}^2$  is centered at  $t = 0$ .

maximum of  $3.75 \times 10^{-17} \text{ cm}^2$  at 105 eV. The experimental results at low energies, recently summarized by Shah *et al.*,<sup>62</sup> are shown in Fig. 12(B) and can be represented using a functional form

$$\sigma_i(\epsilon) = \frac{1}{\left(0.029 + \frac{14.63}{\epsilon - 24.6}\right) \sqrt{\epsilon}} (\text{\AA}^2), \quad (5)$$

where  $\epsilon$  is in eV, shown by the solid line and used in the calculations below. The ionization rate is, therefore,

$$K_i(\epsilon) = n\sigma_i(\epsilon) \sqrt{\frac{2\epsilon}{m_e}}. \quad (6)$$

The overall dynamics of electrons during the laser pulse is described in terms of the time evolution of the energy distribution function  $f(\epsilon, t)$ , which represents the number of electrons with kinetic energy between  $\epsilon$  and  $\epsilon + d\epsilon$ .<sup>63</sup> The function obeys the Fokker–Planck equation<sup>59</sup>

$$\frac{\partial f(\epsilon, t)}{\partial t} = - \frac{\partial}{\partial \epsilon} \left[ K_\epsilon(\epsilon) f(\epsilon, t) - D(\epsilon) \frac{\partial f(\epsilon, t)}{\partial \epsilon} \right] + S(\epsilon, t) \quad (7)$$

with the diffusion coefficient along the energy axis  $D(\epsilon)$  determined by the ‘‘step size’’  $U_p \omega_0^2 / (\omega_0^2 + \nu_{coll}^2)$  and frequency of ‘‘jumps’’  $\nu_{coll}$ . The source and sink term  $S(\epsilon, t)$  is given by

$$S(\epsilon, t) = -K_i(\epsilon) f(\epsilon, t) + 4K_i(2\epsilon + \text{I.P.}) f(2\epsilon + \text{I.P.}, t),$$

i.e., each electron disappearing at energy  $2\epsilon + \text{I.P.}$  produces two electrons at  $\epsilon$ . Note that the total number of electrons, calculated as an integral of the distribution function over energy, is not conserved because the model describes multiplication of the electron population.

Equation (7) was solved numerically using the coefficients  $K_\epsilon(\epsilon)$  and  $K_i(\epsilon)$  calculated from the fitted experimental dependences of  $\sigma_s(\epsilon)$  and  $\sigma_i(\epsilon)$ , Eqs. (4) and (5). The Gaussian laser pulse profile was introduced via time-dependent ponderomotive potential  $U_p$  in expressions for

$K_\epsilon(\epsilon)$  and  $D(\epsilon)$ . An example of the dynamical evolution of the distribution function is shown in Fig. 14, for a pulse with peak intensity of  $I = 3 \times 10^{13} \text{ W/cm}^2$  and FWHM of 80 fs. At the front edge of the laser pulse, the electron distribution, initially a  $\delta$ -function at 0 eV, starts spreading to higher energies due to laser heating. When the edge of the distribution reaches above 24.6 eV, the low-energy end of the distribution function starts to fill in due to impact ionization. Because  $\sigma_i(\epsilon) < \sigma_s(\epsilon)$ , an electron will undergo several energy-gaining collisions above the I.P.(He) before ionizing. Thus, at peak laser intensities, a tail of the distribution function extends somewhat beyond 25 eV, which decays rapidly at the end of the pulse. Note that most of the cascade electrons are produced in the second half of the laser pulse.

The model predicts that the laser pulse multiplies the number of ions by  $M = 2^m$ , where  $m$  is the number of generations in the electron cascade developed during the laser pulse. As expected from the general physical features of the model, the numerical solution of Eq. (7) shows that  $m$  is proportional to the energy-gain rate (2), which is proportional to the laser intensity, and to the time during which the laser acts on the system. Thus, overall, the number of produced ions is determined simply by the total energy per laser pulse  $W$  (intensity integrated over the temporal profile of the pulse):<sup>64</sup>  $m = W/W_2$ , and

$$M = 2^{W/W_2}. \quad (8)$$

The characteristic laser power at which the number of ions doubles is predicted to be  $W_2 = 13 \pm 2 \mu\text{J/pulse}$ , i.e., intensity  $I_2 = (1.0 \pm 0.2) \times 10^{13} \text{ W/cm}^2$  for 790 nm pulses of temporal width  $t_0 = 80 \text{ fs}$  and focal area of  $(1.6 \pm 0.3) \times 10^{-5} \text{ cm}^2$  [the main sources of error in the estimate are the experimentally measured beam waist and uncertainties in  $\sigma_s(\epsilon)$ ,  $\sigma_i(\epsilon)$ ]. A cascade time constant  $\tau_c$  may be defined such that  $m = t_0/\tau_c$ . At  $1 \times 10^{13} \text{ W/cm}^2$ , it takes on the average  $\tau_c = 80 \text{ fs}$  for an electron to gain energy and ionize a He atom. The constant decreases inversely proportional to the laser intensity, and at  $I = 4.5 \times 10^{13} \text{ W/cm}^2$   $\tau_c = 16 \text{ fs}$ , i.e., the cascade consists of five generations.

### 1. Power dependence of current and fluorescence

With the identification of the initial concentration of quasifree electrons as the surviving concentration of triplet excimers,  $C_1$ , and under the assumption that the ion pairs generated through the cascade recombine to form the triplet excimer, the source term in the excimer steady state (Fig. 8) becomes

$$C_0 = MC_1, \quad (9)$$

combining this with the bimolecular decay expression (1) expressions for the  $\text{He}_2^*(^3a)$  concentrations characterizing the steady state are easily obtained

$$C_0 = \frac{1}{Kt_1}(M-1),$$

$$C_1 = \frac{1}{Kt_1} \frac{M-1}{M}, \quad (10)$$

to show that at a  $1/t_1$  repetition rate of excitation, the triplet concentration at any time is defined by two parameters: the

multiplication factor  $M$  and the decay constant  $K$ . Since the decay constant is well established independently,<sup>44</sup> the multiplication factor can be uniquely determined from the measured power dependences of the fluorescence and photocurrent on the laser power  $W$  using independently adjusted pump and probe lasers, data of Fig. 11.

We recognize that the fluorescence intensity obtained from the pump beam alone  $S_1(W_{\text{pu}})$  [Fig. 11(a)] is determined by the concentration of triplets that survived from the previous pulse  $C_1$  and the fluorescence excitation efficiency  $\alpha(W_{\text{pu}})$ :

$$S_1(S_{\text{pu}}) = \frac{1}{Kt_1} \frac{M(W_{\text{pu}}) - 1}{M(W_{\text{pu}})} \alpha(W_{\text{pu}}). \quad (11)$$

In the case of fluorescence in pump-probe measurements we must include the production of excimers by both pump and probe pulses. This changes expressions (10) for  $C_0$  and  $C_1$  in which the multiplication factor  $M$  is now substituted by  $M(W_{\text{pu}})M(W_{\text{pr}})$ . The pump-probe fluorescence signal  $S_2(W)$  [Fig. 11(b)] arises from the freshly generated excimers, 1 ns after the generation pulse, i.e., reflects concentration  $C_0$  (the fluorescence excitation efficiency factor in this case is determined by the probe intensity, i.e., is a constant), and also includes the signal (although small) from the concentration  $C_1$  excited by the pump:

$$S_2(W_{\text{pu}}) = \frac{1}{Kt_1} \left\{ \left[ M(W_{\text{pu}}) - \frac{1}{M(W_{\text{pr}})} \right] \alpha(W_{\text{pr}}) + \left[ 1 - \frac{1}{M(W_{\text{pu}})M(W_{\text{pr}})} \right] \alpha(W_{\text{pu}}) \right\}. \quad (12)$$

For the experimentally realized case  $M(W_{\text{pu}}), M(W_{\text{pr}}) \gg 1$  (see below), and  $S_2(W_{\text{pu}}) \propto M(W_{\text{pu}})$ .

The current  $i(W_{\text{pu}})$  [Fig. 11(c)] measures the number of produced ions, which is proportional to concentration  $C_0$  of the generated excimers,

$$i(W_{\text{pu}}) \propto \frac{[M(W_{\text{pu}})M(W_{\text{pr}}) - 1]^2}{M(W_{\text{pu}})M(W_{\text{pr}})}, \quad (13)$$

and, like the pump-probe fluorescence signal, is approximately proportional to  $M(W_{\text{pu}})$ .

Recall that the 790 nm induced fluorescence from the triplet excimer is a two-photon process, therefore, the fluorescence excitation efficiency is quadratic in laser power:  $\alpha(W) \propto W^2$ . According to Eq. (8), the multiplication of the triplets by the electron avalanche ionization is exponential in laser power. With the substitution of this functional form in Eqs. (11)–(13), the experimental power dependence of Fig. 11 can be reproduced, as shown by the solid curves in Fig. 11. The values of  $M(W_{\text{pr}})$ ,  $\alpha(W_{\text{pr}})$  for the probe pulse, which enter Eqs. (12) and (13) for  $S_2(W)$  and  $i(W)$  are obtained by substituting the probe pulse power into the optimized  $M(W)$  and  $\alpha(W)$  dependences, and provide a self-consistency check of the fit.

The best fit of the experimental data is achieved for the value of characteristic laser power  $W_2 = 12 \mu\text{J/pulse}$ , i.e.,  $I_2 = 0.9 \times 10^{13} \text{ W/cm}^2$ , in excellent agreement with the theoretically estimated values. The corresponding cascade time constant is  $\tau_c = 18 \text{ fs}$  at  $4 \times 10^{13} \text{ W/cm}^2$ . We note that the

cascade ionization model described in the previous section does not have any adjustable parameters. The experiment implies that at a laser intensity  $I=4.5\times 10^{13}$  W/cm<sup>2</sup>, just below the breakdown threshold, the multiplication factor is  $M=30$ , the characteristic time for the impact ionization is  $\tau_c=16$  fs, and the cascade consists of  $m=5$  generations.

An additional test of the proposed mechanism is provided by the measurements with stretched pulses. The experiments indicate that the signal does not change when the laser pulse is stretched while maintaining the total energy per pulse  $W$  constant. Indeed, from the discussion before Eq. (8) it follows that if the pulse width  $t_0$  is increased and at the same time the peak intensity  $I$  is decreased by the same factor, the multiplication factor will remain exactly the same. This is a unique feature of the electron avalanche multiplication mechanism, which distinguishes it from multiphoton processes.

Finally, we may comment on the laser wavelength dependence of the process. Experimentally, when using the second harmonic of the fs laser at 395 nm, it is observed that the low-intensity excitation regime is compressed, such that fluorescence is only detected near the breakdown threshold. The model predicts that at 395 nm, the electron multiplication time is four times longer. The reason for this is that the ponderomotive potential  $U_p$  in Eq. (2) is inversely proportional to the square of the light frequency, i.e., at a given intensity the energy gain is four times slower for the second harmonic.

### C. Ion recombination

#### 1. Spatial distribution of the ions created by the cascade

The cascade ionization model allows detailed temporal, spatial, and energetic characterization of the electrons and ions prepared by the laser pulse. The average separation between the generated positive ions is equal to the displacement of an electron between the ionization events. Assuming random walk motion of the electron during acceleration, the spatial cascade length  $l_c$  is determined by the scattering length  $l_s$  and the number of collisions  $n_{\text{coll}}$  suffered during energy gain and impact ionization. From the numerical solution of Eq. (2), we obtain the characteristic cascade length at which secondaries are generated

$$l_c = 60 \text{ \AA},$$

independent of laser intensity. The multiplication proceeds around the primary center, and thus creates a clump of  $M$  positive ions separated on the average by  $l_c$ . The distance between clumps is determined by the average separation between the  $\text{He}_2^*$  (<sup>3</sup>*a*) precursors, which, at concentration  $C_1 \sim 10^{12}$  cm<sup>-3</sup> is  $10^4$  \AA. The nascent  $\text{He}^+$  ion undergoes an ultrafast dimerization reaction (also known as charge localization<sup>10</sup>), to form  $\text{He}_2^+$ , on the time scale of 20–200 fs,<sup>33</sup> and subsequently, relaxes vibrationally in collinear collisions with He atoms to form a thermal “snowball” state with a  $\text{He}_3^+$  core. The associated length scale of the hole hopping before localization can be estimated as  $\sim 20$  \AA,<sup>10</sup> and therefore, inhomogeneous spatial distribution will remain after spreading during thermalization.

The thermalization length of the “hot” quasifree electrons is determined by the number of elastic collisions with He atoms (the only mechanism of energy loss for electrons below 20 eV). The energy transfer efficiency is  $\gamma = 2m_e/M_{\text{He}} = 2.7 \times 10^{-4}$  per collision. The number of collisions necessary to dissipate kinetic energy from  $\epsilon_i$  to  $\epsilon_f$  is given as

$$n = \frac{\ln(\epsilon_i/\epsilon_f)}{\ln[1/(1-\gamma)]} \approx \frac{1}{\gamma} \ln(\epsilon_i/\epsilon_f), \quad (14)$$

and is quite insensitive to the assumed initial and final energy. For an electron to trap, it must slow down such that its kinetic energy falls below the potential barrier for passing through the cells of the liquid. Using the electron–He pseudopotential given by Jortner *et al.*,<sup>35</sup> we can estimate the potential corrugation felt by an electron in L-He to be of order 0.2 eV. The average initial kinetic energy of electrons is calculated from the electron energy distribution at the end of the pulse (see Fig. 14)

$$\langle \epsilon \rangle = \int \epsilon f(\epsilon, t = \infty) d\epsilon = 10.4 \text{ eV}. \quad (15)$$

The distribution function  $f(\epsilon, t = \infty)$ , and therefore  $\epsilon_i$ , is nearly independent of the laser intensity. Substituting these values of  $\epsilon_i$  and  $\epsilon_f$  in Eq. (14), we determine the average number of collisions to be of the order of  $n \sim 10^4$ , and corresponding migration length for the nascent electron

$$l_t = l_s n^{1/2} \sim 10^3 \text{ \AA}, \quad (16)$$

in which the average scattering length  $l_s = 10$  \AA is used. The trapped electron thermalizes at the same position as the well-known bubble state, on the time scale estimated by Rosenblit and Jortner as 4–8 ps.<sup>39</sup> The thermal electron bubbles are, therefore, distributed in a diffuse cloud at a distance  $\sim 10^3$  \AA around the positive ion clump.

#### 2. Charge separation by external electric field

The extraction of charge carriers from the excitation volume by a weak external field confirms the picture of spatially separated positive and negative ions described above. We established that the collected charge corresponds to 0.5% of the generated excimer concentration. Under the assumption that all recombined ion pairs form excimers, we may conclude that this fraction corresponds to ions created at a separation where the dc field imposed by the electrodes,  $F_{\text{ext}}$ , exceeds the Coulombic attraction between ions:

$$R_{+/-} = \sqrt{\frac{e}{4\pi\epsilon_0 F_{\text{ext}}}},$$

i.e., the photocurrent yield probes the outer tail of the electron cloud ( $l_t$  distribution). Under the operating conditions of  $F_{\text{ext}} = 200$  V/cm, we calculate  $R_{+/-} = 2.7 \times 10^3$  \AA. Based on the Gaussian distribution of charge separation lengths  $l_t$  imposed by the random scattering events, the measured fraction of extractable charges implies an initial ion separation distance such that  $1 - \text{erf}(R_{+/-}/l_t) = 0.005$ , i.e.,  $l_t \sim 10^3$  \AA, in agreement with the theoretically estimated value (16).

### 3. Recombination time scale

The internuclear separation of the  $\text{He}_2^+$  ion (1.08 Å) (Ref. 65) is very close to that of the  $\text{He}_2^*$  excimer (1.05 Å). Recombination with the thermalized electron is, therefore, expected to populate the Rydberg  $\text{He}_2^*$  states rather than the ground electronic state because of the better Franck–Condon overlap. The observed formation kinetics of the excimers (Fig. 7), determines a 100 ps time scale for ion recombination, which confirms that the produced ions are initially inhomogeneously distributed, as described above. Indeed, homogeneous recombination at an initial concentration  $\sim 10^{13} \text{ cm}^{-3}$  is expected for the 100  $\mu\text{s}$  time scale, based on the diffusion coefficient for the positive and negative ions estimated using the Nernst–Einstein relation. The process consists of two stages: diffusional drift of the ions in the attractive Coulomb field and contact recombination which populates the  $\text{He}_2^*(^3a)$  state. Due to the strong field (of the order of  $10^3 \text{ V/cm}$  for separations less than  $10^3 \text{ Å}$ ), the drift velocity of the ions may approach the Landau limit ( $v_L \approx 60 \text{ m/s}$ ), above which the mobility drastically reduces.<sup>34</sup> This limits the estimated drift time from the initial separation distance of  $10^3 \text{ Å}$  to  $\sim 1 \text{ ns}$ . An initial rapid expansion of the positive ion clump due to Coulombic repulsion may facilitate the kinetics. Further experiments are needed to elucidate the limiting process which determines the observed overall recombination time scale.

### 4. Breakdown

With regard to breakdown, the signatures of which were described in Sec. II A, two important observations can be made by inspecting the data in Fig. 11. First, the photocurrent curve as a function of intensity shows no discontinuities, implying that there is no abrupt change in the extractable number of photogenerated ions, as would be expected in a runaway avalanche. The second important observation is that the (LIF) signal degrades at breakdown, both for pump alone and pump–probe signals, implying that laser scattering occurs within the pulse width of 80 fs, and therefore, breakdown is sensed optically on that time scale. Consistent with this, we note that white-light generation from the laser tracks the intensity of emissions attributed to breakdown. These observations allow insights into the microscopics of the initiation of breakdown. With 30–40 ions created on a length scale of 60 Å just below breakdown, clearly, the new generation of electrons can now be expected to be trapped by the positively charged clump. Light scattering and white-light generation within the pulse can be understood in terms of radiation coupled to interacting electron–ion pairs, i.e., accelerated dipoles supporting a continuum of radiative states. The Coulombically trapped electron–ion pairs constitute a plasma that can be strongly heated by the radiation field. Evidently, breakdown, and the subsequent Coulomb explosion, which leads to cavitation and bubble formation, is initiated in clumps containing a total of 30–40 ion pairs.

### D. Overall mechanism for excimer multiplication

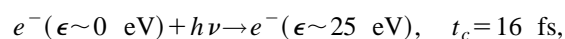
Based on the above discussion, we can reconstruct the mechanism for maintenance of the steady state in triplet ex-

cimers. The requisite steps, and where applicable their time and length scales, are given below for a laser intensity of  $I = 4.5 \times 10^{13} \text{ W/cm}^2$ , i.e., just below breakdown:

(1) The radiation suppresses the Coulomb barrier for the Rydberg electron of the  $\text{He}_2^*(^3a)$  excimer rendering it into a quasifree state at  $\sim 0 \text{ eV}$ :

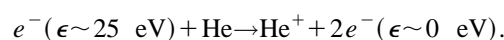


(2) During the laser pulse, the quasifree electrons are ponderomotively accelerated, and gain kinetic energy in collisions with the He atoms of the liquid:



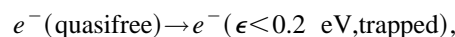
$$l_c = 60 \text{ Å},$$

electrons with energy  $\epsilon \geq 24.6 \text{ eV}$  ionize He atoms and generate secondaries:

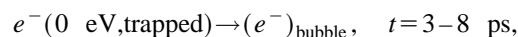


This autocatalytic cycle repeats within the laser pulse, multiplying the quasifree electron concentration by a factor of  $M = 2^m$ , where  $m$  is the number of cycles.

(3) Upon termination of the laser pulse, the “hot” quasifree electrons slow down and are eventually trapped in density minima of the liquid, then fully thermalize and form the “bubble” state due to the repulsive exchange interaction with the surrounding ground-state He atoms<sup>35,36</sup>

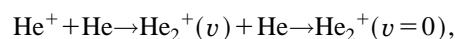


$$t_t \sim 10\text{--}20 \text{ ps}, \quad l_t \approx 10^3 \text{ Å},$$



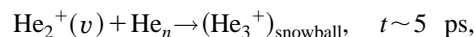
where the bubble formation time scale is from the theoretical analysis of Rosenblit and Jortner,<sup>39</sup> and assumes an initial thermal electron.

(4) The dimerization of the positive helium ion



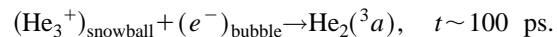
$$t = 100\text{--}500 \text{ fs}, \quad l \sim 20 \text{ Å},$$

proceeds via hole hopping until localization through vibrational relaxation of the dimer ion via formation of a linear intermediate  $[\text{He}_3^+]$ .<sup>33</sup> The length scale associated with this process is that of hole migration, modeled theoretically<sup>66</sup> and recently determined experimentally in He clusters.<sup>10</sup> After complete vibrational relaxation, the triatomic ion is stabilized as the core of the snowball,<sup>41</sup> which is created by the charge-induced polarization of the neighboring shells,



where the time scale is that of complete thermalization of the ionic core, and is estimated from simulations.

(5) The thermalized ions recombine, forming the vibrationally relaxed triplet exciplex as a major channel:



The time scale is that observed experimentally (formation dynamics in Fig. 7).

Once the steady-state concentration of the triplet excimers is established, it is maintained in the sequence of pro-

cesses (1)–(5). The initial buildup of the steady-state concentration, however, requires an initial finite concentration of seed electrons. Experimentally, we could only establish that near-breakdown threshold, at  $I=4.5\times 10^{13}$  W/cm<sup>2</sup>, the steady state (SS) is reached in less than five pulses. The required seed concentration  $C_s$  to reach the SS concentration of  $C_0$  in  $n$  pulses can be obtained by noting that  $C_0 = M^n C_s = 2^{m+n} C_s$ , where  $m$  is the number of generations in the cascade, in each pulse. Near breakdown, where  $m=5$ , a seed concentration of  $10^{10}$  cm<sup>-3</sup> is sufficient to reach the steady state in  $n=5$  pulses. Extrapolation of the gas-phase data on laser ionization of He (Ref. 27) yields an ionization probability of  $\sim 10^{-12}$  under our conditions. Although extremely small, this is still enough to produce  $\sim 10^{10}$  cm<sup>-3</sup> ions in the excitation volume (the liquid-helium number density is  $2.2\times 10^{22}$  cm<sup>-3</sup>), enough to initiate the steady state. Note, however, that any impurity with I.P. $<5$  eV can act as a seed, and the requisite concentration implies that an impurity level of one part in  $10^{12}$  is sufficient for the task. Thus, it is difficult to give a unique identity of the seed.

## V. CONCLUDING REMARKS

Our experimental results demonstrate controlled excitation of the superfluid helium that may be achieved using intense femtosecond laser pulses. Ionization of the liquid, which constitutes the main step in the excitation sequence, is accomplished below the laser breakdown threshold by a subcritical electron avalanche. Only up to five generations of ionizing electrons develop, owing to the ultrashort pulse width, high ionization potential of He, and the absence of energy levels below 18 eV. This situation is to be contrasted to the usually observed laser breakdown induced by longer pulses and/or in media with a narrower band gap, which is characterized by a runaway fully developed avalanche with up to 30 generations. Shot-to-shot irreproducibility of the number of produced ions in this regime, together with the onset of strong optical nonlinearities in the generated dense plasma, renders spectroscopic studies impossible. As a consequence, the laser breakdown studies usually provide only one experimental observable, that is, the threshold intensity, thus limiting the possibility of comparing predictions of the avalanche ionization model with experiment. Laser-induced breakdown has many important applications in areas ranging from remote chemical sensing to eye surgery.<sup>67,68</sup> Femtosecond ionization cascade in liquid helium is a unique testing ground, which provides detailed characterization of the onset of the breakdown via an experimentally measured number of produced ions as a function of laser intensity. Our results provide a microscopic picture of the cascade development, indicating that the breakdown is initiated in tight clumps of  $\sim 30$ – $40$  ions with an interionic separation of  $\sim 60$  Å dictated by the characteristic travel distance required for an electron to reach a kinetic energy of I.P. $=25$  eV.

The described excitation mechanism allows sudden access to a variety of excited states, whose time-resolved spectroscopy may provide significant insights into the microscopic dynamics of the superfluid helium. Initial thermalization of the nascent excess electron and positive ion involve ultrafast nonadiabatic dynamics, which are expected

to provide a rigorous test for the existing semiclassical treatments due to the highly quantum nature of He motions. The subsequent recombination of the thermalized ions presents a considerable interest as a prototype electron transfer system in a nonpolar solvent. Finally, the neutral He<sub>2</sub>(<sup>3</sup>*a*) excimers generated in the liquid are a convenient spectroscopic probe. Impulsive electronic excitation of these Rydberg molecules, which allows us to follow the motions of the surrounding superfluid in real time, will be presented in a separate report.

## ACKNOWLEDGMENT

This research was made possible through a grant from the U.S. AFOSR (F49620-95-1-0213).

- <sup>1</sup>T. Yabuzaki, T. Kinoshita, K. Fukuda, and Y. Takahashi, *Z. Phys. B* **98**, 367 (1995); **98**, 387 (1995); **98**, 391 (1995); A. Fujisaki, K. Sane, T. Kinoshita, Y. Takahashi, and T. Yabuzaki, *Phys. Rev. Lett.* **71**, 1039 (1993).
- <sup>2</sup>Q. Hui, J. L. Persson, J. H. M. Beijersbergen, and M. Takami, *Z. Phys. B* **98**, 353 (1995); J. H. M. Beijersbergen, Q. Hui, and M. Takami, *Phys. Lett. A* **181**, 393 (1993).
- <sup>3</sup>H. Günther, G. zu Putlitz, and B. Tabbert, *Z. Phys. B* **98**, 297 (1995); H. Günther, M. Foerste, C. Hönninger, G. zu Putlitz, and B. Tabbert, *ibid.*, **98**, 395 (1995); B. Tabbert, M. Beau, H. Günther, W. Häußler, C. Hönninger, K. Meyer, B. Plagemann, and G. Zu Putlitz, *ibid.* **97**, 425 (1995).
- <sup>4</sup>S. Grebnev, J. P. Toennies, and A. Vilesov, *Science* **279**, 2083 (1998).
- <sup>5</sup>J. Harms, M. Hartmann, J. P. Toennies, A. Vilesov, and B. Sartakov, *J. Mol. Spectrosc.* **185**, 204 (1997); M. Hartmann, R. E. Miller, J. P. Toennies, and A. Vilesov, *Phys. Rev. Lett.* **75**, 1566 (1995).
- <sup>6</sup>K. K. Lehman and G. Scoles, *Science* **279**, 2065 (1998).
- <sup>7</sup>F. Stienkemeier, J. Higgins, W. E. Ernst, and G. Scoles, *Phys. Rev. Lett.* **74**, 3592 (1995).
- <sup>8</sup>J. Higgins, C. Callegari, J. Reho, F. Stienkemeier, W. E. Ernst, K. K. Lehman, M. Gutowski, and G. Scoles, *Science* **273**, 629 (1996).
- <sup>9</sup>M. Behrens, U. Buck, R. Frochtenicht, M. Hartmann, and M. Havenith, *J. Chem. Phys.* **107**, 7179 (1997).
- <sup>10</sup>B. E. Callicoatt, K. Forde, T. Ruchti, L. Jung, K. C. Janda, and N. Halberstadt, *J. Chem. Phys.* **108**, 9371 (1998); B. E. Callicoatt, D. D. Mar, V. A. Apkarian, and K. C. Janda, *ibid.* **105**, 7872 (1996).
- <sup>11</sup>R. Frochtenicht, M. Kaloridis, M. Koch, and F. Huisken, *J. Chem. Phys.* **105**, 6128 (1996).
- <sup>12</sup>K. B. Whaley, in *Advances in Molecular Vibrations and Collision Dynamics*, edited by J. Bowman (JAI, Greenwich, CT, 1988), Vol. III.
- <sup>13</sup>P. L. Kapitza, *Nature (London)* **141**, 74 (1938).
- <sup>14</sup>J. Wilks and D. S. Betts, *An Introduction to Liquid Helium* (Clarendon, London, 1987).
- <sup>15</sup>L. Tisza, *Nature (London)* **141**, 913 (1938), *C. R. Acad. Sci. Paris* **207**, 1035 (1938); *ibid.* **207**, 1186 (1938).
- <sup>16</sup>L. D. Landau, *J. Phys. (Moscow)* **5**, 185 (1941); *ibid.* **11**, 91 (1947).
- <sup>17</sup>E. L. Andronikashvili, *J. Phys. (Moscow)* **10**, 201 (1946).
- <sup>18</sup>E. Cheng, M. A. McMahon, and K. B. Whaley, *J. Chem. Phys.* **104**, 2669 (1996); Y. Kwon, D. M. Ceperley, and K. B. Whaley, *ibid.* **104**, 2341 (1996); M. V. Rama Krishna and K. B. Whaley, *ibid.* **93**, 6738 (1990); **93**, 746 (1990).
- <sup>19</sup>M. Lewerenz, B. Schilling, and J. P. Toennies, *Chem. Phys. Lett.* **206**, 381 (1993).
- <sup>20</sup>M. Hartmann, R. E. Miller, J. P. Toennies, and A. Vilesov, *Science* **272**, 1631 (1996).
- <sup>21</sup>D. M. Brink and S. Stingari, *Z. Phys. D* **15**, 257 (1990).
- <sup>22</sup>S. Kanorsky, A. Weis, M. Arndt, R. Dziejwior, and T. W. Hansch, *Z. Phys. B* **98**, 371 (1995); **98**, 377 (1995).
- <sup>23</sup>R. Zadoyan, J. Almy, and V. A. Apkarian, *J. Chem. Soc. Faraday Discuss.* **108**, 255 (1997).
- <sup>24</sup>P. Dietrich, N. H. Burnett, M. Ivanov, and P. B. Corkum, *Phys. Rev. A* **50**, R3585 (1994).
- <sup>25</sup>See the recent review by F. Krausz, T. Brabec, M. Schürer, and C. Spielman, *Opt. Photonics News* **9**, 46 (1998).
- <sup>26</sup>L. V. Keldysh, *Sov. Phys. JETP* **20**, 1307 (1965).
- <sup>27</sup>B. Walker, B. Sheehy, L. F. DiMauro, P. Agostini, K. J. Schaefer, and K. C. Kulander, *Phys. Rev. Lett.* **73**, 1227 (1994).

- <sup>28</sup>S. August, D. Strickland, D. D. Meyerhofer, S. L. Chin, and J. H. Eberly, *Phys. Rev. Lett.* **63**, 2212 (1989).
- <sup>29</sup>S. August, D. D. Meyerhofer, D. Strickland, and S. L. Chin, *J. Opt. Soc. Am. B* **8**, 858 (1991).
- <sup>30</sup>A. McPherson, B. D. Thompson, A. B. Borisov, K. Boyer, and C. K. Rhodes, *Nature (London)* **370**, 631 (1994).
- <sup>31</sup>E. M. Snyder, S. A. Buzza, and A. W. Castleman, *Phys. Rev. Lett.* **77**, 3347 (1996).
- <sup>32</sup>B. Space and D. F. Coker, *J. Chem. Phys.* **96**, 652 (1992); **94**, 1976 (1991).
- <sup>33</sup>M. Ovchinnikov, B. L. Grigorenko, K. C. Janda, and V. A. Apkarian, *J. Chem. Phys.* **108**, 9351 (1998).
- <sup>34</sup>L. Mayer and F. Rief, *Phys. Rev.* **110**, 279 (1958); *Phys. Rev. Lett.* **5**, 1 (1960); *Phys. Rev.* **119**, 1164 (1960).
- <sup>35</sup>J. Jortner, N. R. Kestner, S. A. Rice, and M. H. Cohen, *J. Chem. Phys.* **43**, 2614 (1965); **43**, 2625 (1965); B. E. Springett, M. H. Cohen, and J. Jortner, *Phys. Rev.* **159**, 183 (1967).
- <sup>36</sup>W. B. Fowler and D. L. Dexter, *Phys. Rev.* **176**, 337 (1968); T. Myakawa and D. L. Dexter, *Phys. Rev. A* **1**, 513 (1969).
- <sup>37</sup>C. C. Grimes and G. Adams, *Phys. Rev. B* **41**, 6366 (1990); **45**, 2305 (1992).
- <sup>38</sup>S. V. Pereverzev and A. Ya. Parshin, *Physica B* **197**, 347 (1994); *Sov. Phys. JETP* **74**, 68 (1992); *JETP Lett.* **52**, 282 (1990).
- <sup>39</sup>M. Rosenblit and J. Jortner, *J. Phys. Chem.* **101**, 751 (1997); *Phys. Rev. Lett.* **75**, 4079 (1995).
- <sup>40</sup>K. R. Atkins, *Phys. Rev.* **116**, 1339 (1959).
- <sup>41</sup>H. Haberland, B. V. Issendorff, R. Frochtenicht, and J. P. Toennies, *J. Chem. Phys.* **102**, 8773 (1995).
- <sup>42</sup>C. M. Surko and F. Reif, *Phys. Rev.* **175**, 229 (1968).
- <sup>43</sup>W. S. Dennis, E. Durbin, Jr., W. A. Fitzsimmons, O. Heybey, and G. K. Walters, *Phys. Rev. Lett.* **23**, 1083 (1969).
- <sup>44</sup>J. W. Keto, F. J. Soley, M. Stockton, and W. A. Fitzsimmons, *Phys. Rev. A* **10**, 872 (1974); **10**, 887 (1974).
- <sup>45</sup>J. W. Keto, M. Stockton, and W. A. Fitzsimmons, *Phys. Rev. Lett.* **28**, 792 (1972).
- <sup>46</sup>M. Stockton, J. W. Keto, and W. A. Fitzsimmons, *Phys. Rev. A* **5**, 372 (1972).
- <sup>47</sup>J. C. Hill, O. Heybey, and G. K. Walters, *Phys. Rev. Lett.* **26**, 1213 (1971).
- <sup>48</sup>M. Joppien, R. Karnbach, and T. Moller, *Phys. Rev. Lett.* **71**, 2654 (1993).
- <sup>49</sup>N. Schwentner, E.-E. Koch, and J. Jortner, *Electronic Excitations in Condensed Rare Gases* (Springer, Berlin, 1985).
- <sup>50</sup>R. H. Day, P. Lee, E. B. Salomon, and D. J. Nagel, *J. Appl. Phys.* **52**, 6965 (1981); B. L. Henke, J. P. Knauer, and K. Premarante, *ibid.* **52**, 1509 (1981).
- <sup>51</sup>W. Qin, K. Minami, A. W. DeSilva, F. Tomimoto, and K. Sato, *Jpn. J. Appl. Phys., Part 1* **36**, 4474 (1997).
- <sup>52</sup>C. M. Surko, R. E. Packard, G. J. Dick, and F. Reif, *Phys. Rev. Lett.* **24**, 657 (1970).
- <sup>53</sup>G. Winterling, W. Heinicke, and K. Dransfeld, *Phys. Rev.* **185**, 285 (1969).
- <sup>54</sup>I. I. Abrikosova and N. S. Skrypnik, *Sov. Phys. JETP* **32**, 34 (1970); I. I. Abrikosova and B. V. Anshukov, *ibid.* **37**, 579 (1973).
- <sup>55</sup>I. I. Abrikosova and A. I. Shal'nikov, *Prib. Tekh. Eksp.* **2**, 242 (1970).
- <sup>56</sup>S. Neeser, R. Tietz, M. Schultz, and H. Langhoff, *Z. Phys. D* **31**, 61 (1994).
- <sup>57</sup>We also note that the first allowed optical transition of He is  $1s^1S \rightarrow 2p^1P$  at 21.3 eV, i.e., it would minimally require the simultaneous absorption of 14 photons.
- <sup>58</sup>L. V. Keldysh, *Sov. Phys. JETP* **20**, 1307 (1965).
- <sup>59</sup>Ya. B. Zel'dovich and Yu. P. Raiser, *Sov. Phys. JETP* **20**, 772 (1965).
- <sup>60</sup>G. A. Askar'yan and M. S. Rabinovich, *Sov. Phys. JETP* **21**, 190 (1965).
- <sup>61</sup>D. E. Golden and H. W. Bandel, *Phys. Rev.* **138**, A14 (1965).
- <sup>62</sup>M. B. Shah, D. S. Elliot, P. McCallion, and H. B. Gilbody, *J. Phys. B* **21**, 2751 (1988).
- <sup>63</sup>For treatment of electron avalanche in laser breakdown using the Fokker-Planck equation, see, e.g., B. C. Stuart, M. D. Feit, S. Herman, A. M. Rubenchik, B. W. Shore, and M. D. Perry, *Phys. Rev. B* **53**, 1749 (1996).
- <sup>64</sup>As mentioned above, this remains true as long as the laser intensity is high enough, so that the electron heating rate is higher than elastic energy losses and that the seed electrons are produced via Coulomb barrier suppression of  $\text{He}_2^*(^3a)$ .
- <sup>65</sup>G. Herzberg, *Spectra of Diatomic Molecules* (Van Nostrand Reinhold, New York, 1950).
- <sup>66</sup>N. Halberstadt and K. C. Janda, *Chem. Phys. Lett.* **282**, 409 (1998).
- <sup>67</sup>K. Song, Y. I. Lee, and J. Sheddou, *Appl. Spectrosc. Rev.* **32**, 183 (1997).
- <sup>68</sup>S. J. Gitomer and R. D. Jones, *IEEE Trans. Plasma Sci.* **19**, 1209 (1991).
- <sup>69</sup>K. Kimura, *Chem. Phys.* **84**, 2002 (1986).